Hall D KLF E12–19–001
Intermediate Experiment Readiness Review
Jefferson Lab, August 29-30, 2024

KLF Collaboration

August 22, 2024

Contents

Abstract

This intermediate K-Long Facility Experiment Readiness Review aims to demonstrate the feasibility of the key objectives of the experiment using a proton target under real experimental conditions. [https://wiki.jlab.org/klproject/index.php/KLF$_-$Phase$_-$Intermediate$_-$ERR].

1 Trigger and Data Volume

Details of the trigger and data volume are given in the following subsections.

1.1 Trigger

For the KLF experiment [M. Amaryan *et al.* arXiv:2008.08215 [nucl-ex]], we propose using a simple trigger based on energy depositions in barrel calorimeters (BCAL) and forward calorimeters (ECAL / FCAL). The ECAL is a new lead tungsten calorimeter consisting of 1596 high-resolution, high-granularity crystals, which replaced the inner part of the GlueX forward lead glass calorimeter. This calorimeter-based trigger has been successfully employed in other GlueX experiments, including the recent GlueX-II experiment at high luminosity. During high-intensity production runs, the typical trigger rate was about 70 kHz, resulting in a data rate of 1.4 Gb/sec.

Many physics reactions produced by the K_L-proton interactions predominantly involve charged particles in the final state. To achieve a high trigger efficiency (close to unity) for such reactions, the calorimeter energy thresholds must be set below the energy response of minimum ionizing particles. At the same time, the trigger must reject events caused by background neutrons and low-energy photons incident on the liquid hydrogen (LH2) target.

Background rejection and trigger efficiency for the reactions of interest were studied using a detailed Geant4 detector simulation. In this simulation, the standard geometry of the GlueX detector was modified to include the realistic geometry of the LH2 target cell (6 cm in diameter and 40 cm long) and the new forward calorimeter (ECAL/FCAL). The detector geometry will be described in Section 2. Background neutrons and photons, generated according to the realistic energy spectra described in the KLF proposal, were inputted into Geant. The background particles were uniformly distributed on the face of the LH2 target, based on background studies using the MCNP program. The total integrated flux of neutrons and photons was 6.6×10^6 n/sec and 2×10^8 γ/sec, respectively.

Background	Rates in sub-detectors (kHz)			
	BCAL	ECAL/FCAL	BCAL + ECAL/FCAL	Start Counter
Neutron	11.7	13.0	24.2	42.8
Photons	≪ 1	≪ 1	≪ 1	5.8×10^3

Table 1: Rate in the GlueX sub-detectors induced by the neutron and photon backgrounds.

The calorimeter rates induced by the background are presented in Table 1. For BCAL, an energy threshold per cell of 20 MeV was applied, with the total energy deposition required to be greater than 100 MeV. In the forward calorimeter the per cell energy thresholds in the ECAL and FCAL were set to 20 MeV and 130 MeV, respectively. [1] The total energy deposition in the forward direction was required to be $E_{\mathrm{ECAL}} + E_{\mathrm{BCAL}} >$ 100 MeV. The column "BCAL + ECAL / FCAL" in the Table represents the rate of events where the energy sum in the forward and barrel calorimeters exceeds 100 MeV, which corresponds to the proposed trigger criteria. The trigger rate produced by the neutron background is estimated to be about 24 kHz, with approximately 12 kHz contributed by the BCAL. The dominant contribution to this rate originates from the neutron-proton elastic scattering process, the cross section of which was measured to be approximately 34 mb in the neutron energy range around 0.5 GeV [V. P. Dzhelepov, B. M. Golovin, Iu. M. Kazarinov, N. N. Semenov, https://cds.cern.ch/record/1241659/files/p115.pdf]. Although the scattering in the center-of-mass system is primarily directed forward and backward, a significant fraction of the scattered protons and neutrons are deflected at relatively large angles in the laboratory frame, producing hits in the detector

---

[1]The larger threshold the FCAL is required because of the excessive noise from Cockcroft Walton bases used for the instrumentation of the FCAL PMTs.

(specifically, about 20% of the protons scatter at polar angles greater than 10 degrees in the laboratory frame, with a transverse momentum greater than 0.22 GeV/c).

The low-energy photon background does not deposit energy in the calorimeters above the set thresholds. However, the large cross section of Compton scattering at these low energies results in a relatively high rate in the Start Counter (SC), making it impractical to use the SC as a standalone detector in the trigger. In particular, approximately half of the beam and background particles pass through the SC detector material due to the smaller size of the SC hole (2 cm in diameter) in the forward direction compared to the beam size.

The total rate of hadronic interactions induced by the K_L beam is less than 1 kHz, which is comparable to the rate of cosmic rays detected by the BCAL. Both of these contributions to the overall trigger rate are small. We estimate the total trigger rate to be approximately 26 kHz, which is about 2.5 times lower than the maximum trigger rate of the GlueX detector.
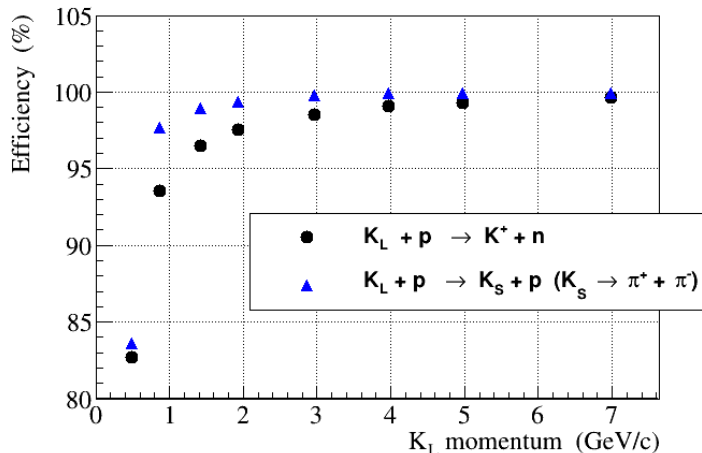

Figure 1: Trigger efficiency for $K_L p \to K^+ n$ and $K_L p \to K_S p$ ($K_S \to \pi^+ \pi^-$) reactions as a function of the K_L momentum.

The trigger efficiency for the reactions $K_L p \to K^+ n$ and $K_L p \to K_S p$ ($K_S \to \pi^+ \pi^-$) as a function of the momentum K_L is presented in Fig. 1. In calculating the efficiency, we select events with reconstructed charged tracks in the final state and verify whether the energy deposition in the calorimeters satisfies the trigger requirements. We expect the lowest efficiency among the key channels to be for the $K_L p \to K^+ n$ reaction, as it involves only one charged kaon and a neutron in the final state. As anticipated, the efficiency is lower (around 83%) at small K_L beam momentum, close to the production threshold, due to the relatively lower energies carried by the particles. The efficiency increases and approaches almost 100% at higher beam momenta, which correspond to the kinematic regions most populated of the K_L beam. The trigger efficiencies for key analysis channels within the K_L momentum range of 1.5 GeV/c and 4.5 GeV/c are listed in Table 2, with values close to 100%.

Channel	Efficiency (%)
$K_L p \to K^+ n$	98.1
$K_L p \to p K_S$ $(K_S \to \pi^+ \pi^-)$	99.6
$K_L p \to \pi^+ \Lambda$	99.4
$K_L p \to K^+ \Xi^0$ $(\Xi^0 \to \Lambda \pi^0)$	100
$K_L p \to \pi^+ \Sigma^0$ $(\Sigma^0 \to \Lambda \pi^0)$	99.9
$K_L p \to p K^*$ $(K^* \to K^+ \pi^-)$	99.7

Table 2: Trigger efficiency for reactions of interest produced by the K_L beam with the momentum between 1.5 GeV/c and 4.5 GeV/c.

1.2 Data Volume

The data volume required for the experiment is defined by three factors - beam flux, cross section, and average event size. One can subdivide expected data volume into 3 different cases - K_L-induced, neutron-induced, and photon-induced.

A K_L related cross section on the neutron is much higher than on the proton, due to allowed isospin $I = 0$, Λ^* states, therefore a K_L induced rate on the deuteron target will be much higher than on the proton. To evaluate K_L-related rates we used a more elaborated $K^- d$ total cross section and a standard KLF K_L flux of 10^4 kaons/s. It resulted in **960 events/s** or rounding up ~ 1 kHz of the kaon-induced data rate. Assuming 10 kb/event, we have about 10 Mb/s = 35 Gb/hour = **850 Gb/day** event rate. About an order of magnitude smaller than currently achievable at GlueX-II.

Neutron-induced reactions can be subdivided into elastic and inelastic reactions. We used SAID cross-section parameterizations [R. A. Arndt, W. J. Briscoe, I. I. Strakovsky, and R. L. Workman, Phys. Rev. C **76**, 025209 (2007)] and a neutron flux from the KLF proposal to evaluate the neutron event rate. Inelastic reactions totaled **233 events/s**.

A tungsten plug reduces photon flux very effectively, leading to a rather small photon-induced reaction rate of about 4 events/s. This leads to a very small contribution to a data storage budget.

We plan to operate with rather open triggers, since some of our channels end up with a fully neutral final state, especially on a neutron target. That is why we also need to take into account cosmic rays rate as a part of our rate/data budget. From previous measurements cosmic production ~ 500 Hz of events when triggered on calorimeters.

The results of the event yields for three cases are presented in Fig. 2. An overall data budget for these cases is expected to be below **1 Tb/day**.

As one learn from from Section 1.1, the only large contributor to a total event budget is a low-energy neutron-proton elastic scattering. Neutron-proton elastic collisions have very strong forward-backward peaking behavior with one particle going to a beam-pipe and another flying at a 90 degree polar angle with close to 0 momentum. Such events would not be detected and recorded. However, even a small fraction of events with larger proton angles or neutrons scattered within the calorimeter can produce a significant trigger rate. Such events can be easily filtered out and would not contribute as a background to any of our reactions of interest.

Inclusion of neutron-proton elastic scattering increases a total data budget, but it still stays more than 2.5 times smaller than the data budget at usual GlueX operation.
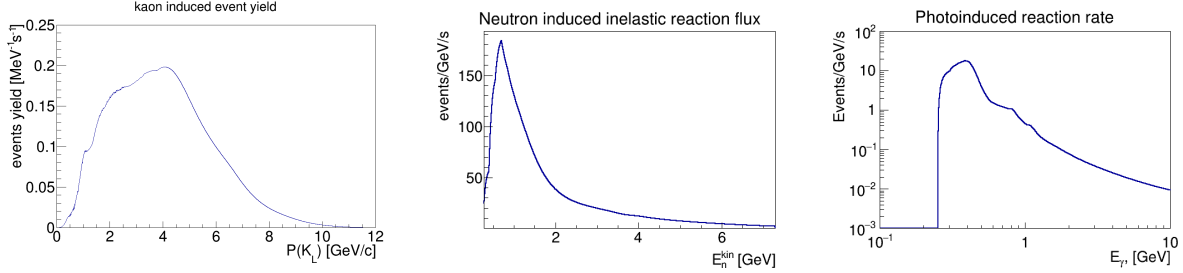
Figure 2: From left to right, Kaon-, neutron-, and photo-induced event yields as a function of beam momentum.

2 Simulation Software

Details of the event generators, K_L beam parameters, neutron and photon beam background, and experiment configuration are given in the following subsections.

2.1 Event Generators

We used several event generators to study the physics channels of interest and their background.

1. *KLGenerator*— This program generates events for the study of excited hyperons, using s-channel reactions of the form $K_L N \to K^0 N$, $K_L N \to (\pi, K)Y^*$, and $nN \to (\pi, K)Y^*$. The final-state particles are distributed according to phase space, since the main purpose of this generator is to determine the experimental acceptance, and most of the hyperons that we are searching for have unknown angular distributions. This generator also has a mode to simulate the backgrounds due to the bleedthrough of beams from other Halls.

2. *KPiGenerator*— Currently, two types of $K\pi$ generators have been prepared for the KLF simulation. The first is for the reaction $K_L p \to K^{*0}(892)p \to K^{\pm}\pi^{\mp}p$. This program is based on the Regge-pole model [G. V. Dass and C. D. Froggatt, Nucl. Phys. B **10**, 151 (1969)] where the Regge pole trajectories for π and a_2 are exchanged in the t channel. In this generator, a relativistic Breit-Wigner is used to simulate the resonance $K^{*0}(892)$, and the kinematics of the decay daughters K and π are simulated uniformly in the phase space of $K^{*0}(892) \to K\pi$. The second generator is for the Δ recoil reaction $K_L p \to K^{*0}(892)\Delta^{++} \to K^-\pi^0 p\pi^+$. For this reaction, the theoretical amplitude and phase of scattering $K\pi$ are provided by [J. R. Pelaez and A. Rodas, Phys. Rev. D **93**, 074025 (2016)]. The low-energy parameters for this model have been tuned to describe the existing $K\pi$ scattering. For the masses of the $K^{*-}(892)$ and Δ^{++} resonances, the relativistic Breit-Wigner shape is used.

A detailed Geant4-based simulation of the KLF beamline in the main hall has recently been developed and can be used to study the properties of the K_L beam and the effect of beam-related backgrounds on the reconstruction of events.

2.2 K_L Beam Parameters

The expected K_L beam parameters were determined by FLUKA simulations of the photon beam interacting with the KPT. The momentum spectrum for K_L's at the face of the cryotarget is shown in Fig. 3.

The K_L beam is currently generated assuming a uniform population of generated events in both the KPT and the cryogenic target, and the generated K_L's are assumed to be moving in the z direction, which is expected to be true to a good approximation.
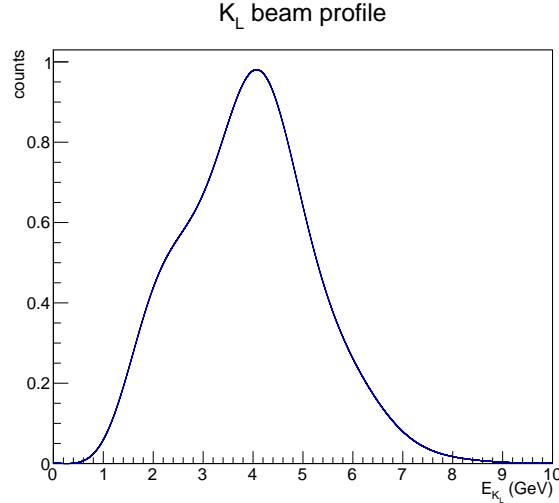
Figure 3: The K_L beam energy spectrum on the face of the cryogenic target used to generate events, as determined by FLUKA simulations.

2.3 Neutron and Photon Beam Background

Neutron-induced reactions have large cross sections. However, in our case, they do not lead to a large background. As explained in previous sections, neutrons lead to ~ 500 Hz of additional data rate. Also, a major part of a neutron-induced total cross section is just elastic scattering with either a very low energetic proton which stops in the target, or a very high energetic proton which fly in the beampipe at an angle close to 0 degrees. The neutron-inelastic reactions are dominated by single- and double- pion production. Neutron-proton reactions can be decomposed into isovector (I = 1) and isoscalar (I = 0) parts. The isovector reactions are extremely well known, because they can be studied in proton-proton collisions. Our knowledge of isoscalar reactions is rather low; however, we know that the isoscalar reaction cross sections are fairly small, compared to the isovector; see Fig. 4 [H. Clement, T. Skorodko, and E. Doroshkevich, Phys. Rev. C **106**, 065204 (2022)].

The energy dependence of the isoscalar neutron-induced reactions is of great interest to hadron physics and heavy-ion communities. The KLF can make an important contribution in this field.

It is also important to mention that due to the large difference in mass and a long flight path from the beryllium kaon production target to the cryogenic reaction target, the neutron- and kaon-induced reactions are largely separated in time; see Fig. 5. Very slow neutrons which tail into subsequent kaon bunches have insufficient energy to produce any reactions, and hence they do not contribute to the background.

2.4 Experiment Configuration

The KLF experiment uses the GlueX spectrometer in its default configuration, as illustrated in Fig. 6 (left). The spectrometer consists of a Start Counter, Central and Forward Drift Chambers, and a Barrel Calorimeter contained inside a solenoid that provides a 2 T magnetic field. Downstream of the solenoid are a DIRC detector, a Time-of-Flight wall, and a Forward Calorimeter. The target volume for the KLF experiment is increased to a diameter of 6 cm and a length of 40 cm a from a diameter of 1.5 cm and a length of 30 cm for the GlueX configuration. This updated cryogenic target geometry has been implemented in GEANT-based simulations, as illustrated in Fig. 6 (right).

We note that the new FCAL insert (ECAL) is not currently included in the default KLF geometry, since it is just being commissioned and its reconstruction software is under active development. As will be shown in Section 4, almost none of the particles of the key final states being studied are produced in the acceptance
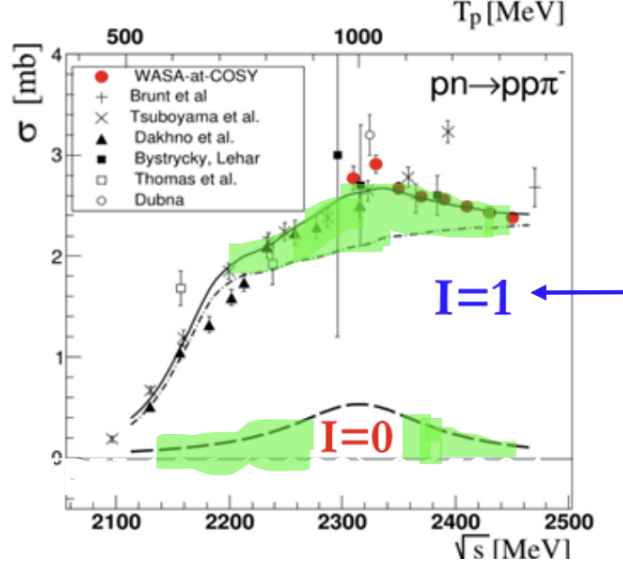
Figure 4: Neutron-induced single pion production cross section separated into isoscalar and isovector parts.
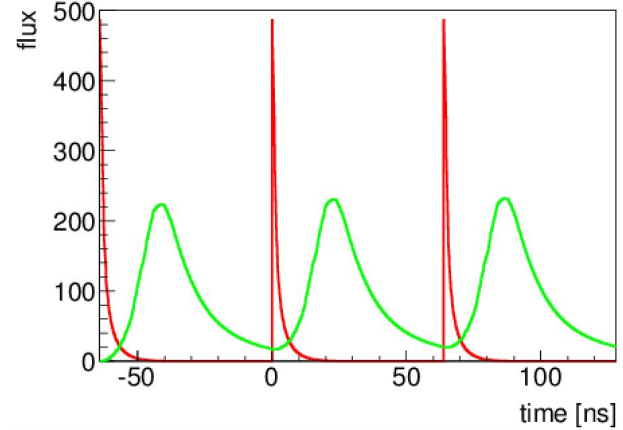

Figure 5: Bunch structure of neutron (green) and kaon (red) induced reactions, under assumptions of 64 ns bunch spacing.

of this subdetector, so it can be neglected for the current studies. We plan to update our software to include this subdetector after it is commissioned in the upcoming experimental run.

3   Reconstruction

The reconstruction and analysis software used for KLF is substantially based on that used for the photon-beam GlueX experiment [S. Adhikari *et al.* Nucl. Instrum. Meth. A **987**, 164807 (2021)]. The various subdetectors are used to reconstruct a similar array of charged and neutral particles, with an emphasis on reconstructing exclusive final states. At KLF energies, most of the particles go into the central part of the detector, where they are well reconstructed. The main difference between the GlueX and KLF reconstruction is in the reconstruction of the beam particles. In the GlueX experiment, the beam photons are measured
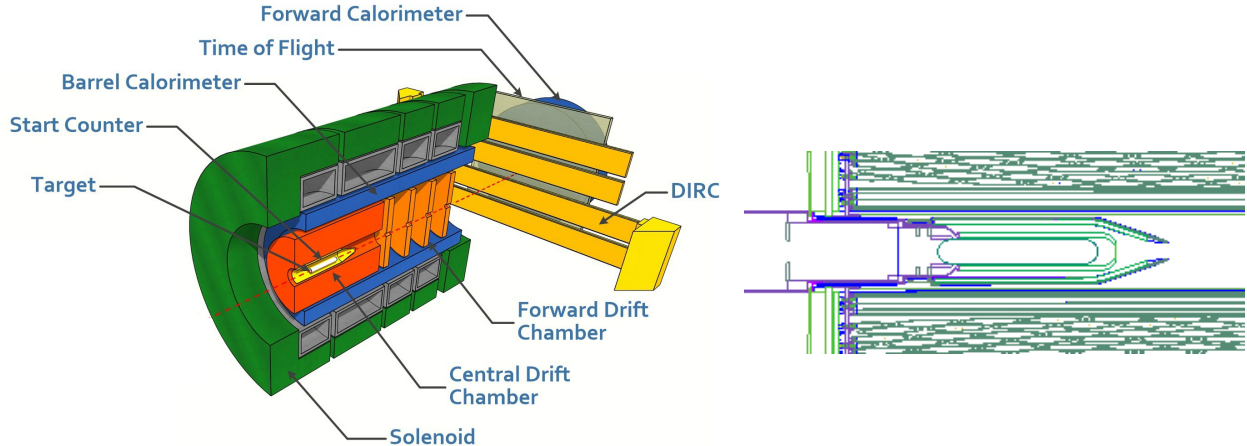
Figure 6: <u>Left</u>: Diagram of GlueX spectrometer. <u>Right</u>: Cross section of geometry from GEANT4-based simulation illustrating the implemented KLF cryogenic target geometry.

in a dedicated detector, and the precise knowledge of the beam photon timing assisted in matching the beam photons with the reconstructed final-state particles and in time-of-flight measurements for particle identification. For the KLF experiment, the reconstructed event vertex in the spectrometer is used to determine the time-of-flight, and therefore the momentum of the K_L beam particle. The quality of the K_L beam reconstruction then depends on the quality of the final-state particle reconstruction.

Details of the reconstruction and calibration are given in the following subsections.

3.1 Calibration Overview

The GlueX spectrometer has been in operation since 2015, and by now the calibration procedures for its subdetectors are generally well developed and understood. All calibration procedures use inclusive samples of single charged particle tracks, photon showers, or $\pi^0 \to \gamma\gamma$ decays, so they can be performed with an untagged beam. Table 3 provides an overview of the calibration procedures performed for GlueX, how often they are performed, and an order-of-magnitude estimate of how much data are required for them.

It is currently planned to take several days of data with a photon beam before the beginning of kaon-beam operations. The detailed specifications of the photon beam are being developed, but it is expected to be of a similar order of magnitude of intensity as current GlueX photon beam operations, although with lower quality. This data will be sufficient to perform an initial calibration of all detector elements with the established GlueX procedures. Data taken with the K_L beam will be sufficient to update the calibrations during data taking, as will be discussed below. Note that most calibrations per run are performed with the equivalent of 1% or less of the data accumulated during the run. The rate of K_L-induced events is expected to be about 1% of the photon-induced rate for GlueX, so we expect to collect enough data to perform these calibrations.

Most calibrations are quite stable on the order of months, aside from rate-dependent effects on detectors close to the beamline. The intensity of beam particles in KLF is several orders of magnitude smaller than that of GlueX, so these rate-dependent effects are expected to be minimal. Notable exceptions include the CDC, whose calibration depends on the ambient temperature and atmospheric pressure. These variations are corrected for every run and have been minimized with the adoption of automated high-voltage tuning for CDC [T. Jeske, D. McSpadden, N. Kalra, T. Britton, N. Jarvis, and D. Lawrence, JINST, **17**, C03043 (2022)]. The gain calibrations of the calorimeters also vary by less than 5% during a run period. This is corrected for by regular recalibration of the calorimeters.

The physical alignment between detector elements is generally very stable, except for the Start Counter,

Detector	Procedure	Est. data required	Frequency
BCAL	per-channel timing	50M events	once
	attenuation length	1B events	once
	z-position	1B events	once
	gains	70M π^0's	monthly
	energy non-linearity	70M π^0's	monthly
CDC	per-channel gain	100M events	once
	overall gain, dE/dx	1M events	per-run
	time-to-distance	1M events	per-run
FCAL	per-channel timing	5M events	per-run
	gains	60M π^0's	weekly-monthly
	energy non-linearity	60M π^0's	weekly-monthly
FDC	per-channel timing	1M events	per-run
DIRC	timing	1M events	per-run
SC	timewalks	10M events	once
	propagation time	100M events	once
TOF	per-channel timing / timewalks	50M events	per-run/several runs
	gains / propagation speed	−	avg. over run
Overall	timing alignment	1M events	per-run

Table 3: Summary of standard calibration procedures for the sub-detectors of the GlueX spectrometer. Also shown is a rough estimate of the amount of data required for each procedure and approximately how often the procedures should be performed during each run period. Data estimation is based on the number of data files that are used for calibrations, where each file contains approximately **1M** triggers, so these estimates should be considered correct to a factor of an order of magnitude.

which is attached to the target assembly and must be resurveyed every time the target is removed and replaced. Periodic surveys of the detector components are used to update the detector geometry. Detailed alignment of the components of the drift chamber is performed using a Millepede-based procedure [N. S. Jarvis *et al.* Nucl. Instrum. Meth. A **962**, 163727 (2020)], and it has been found to be stable for most of the history of the GlueX experiment so far.

3.2 Timing Calibration

The initial timing alignment will be performed with photon beam data taken at the beginning of the experiment and will use standard GlueX procedures. After that, timing calibrations have been observed to be generally stable during a run. The timing alignment will be monitored using standard procedures based on measuring the time-of-flight of individual charged particles or calorimeter showers from the Start Counter or the average event vertex. An example of these distributions is shown for events of reaction $K_L p \rightarrow K_S p$, $K_S \rightarrow \pi^+ \pi^-$, showing that they perform well in Fig. 7.

Additionally, the photon beam data will allow for a precise alignment of the RF signal, and precise determination of the flight time between the KPT and cryogenic target, which is crucial for the accurate measurement of the K_L momentum. This will be performed by comparing the event times measured in the spectrometer with the beam times measured near the KPT position.

3.3 Calorimeter Energy Calibration

An energy calibration of the GlueX calorimeters is performed with photons originating from $\pi^0 \rightarrow \gamma\gamma$ decay. The source of π^0 is not important as long as sufficient statistics with momenta larger than 200 MeV/c, known production vertex, and signal over-background greater than 1 can be collected over the full angular range. There are several sources of neutral pions - decays of excited hyperons, decays of excited kaons,
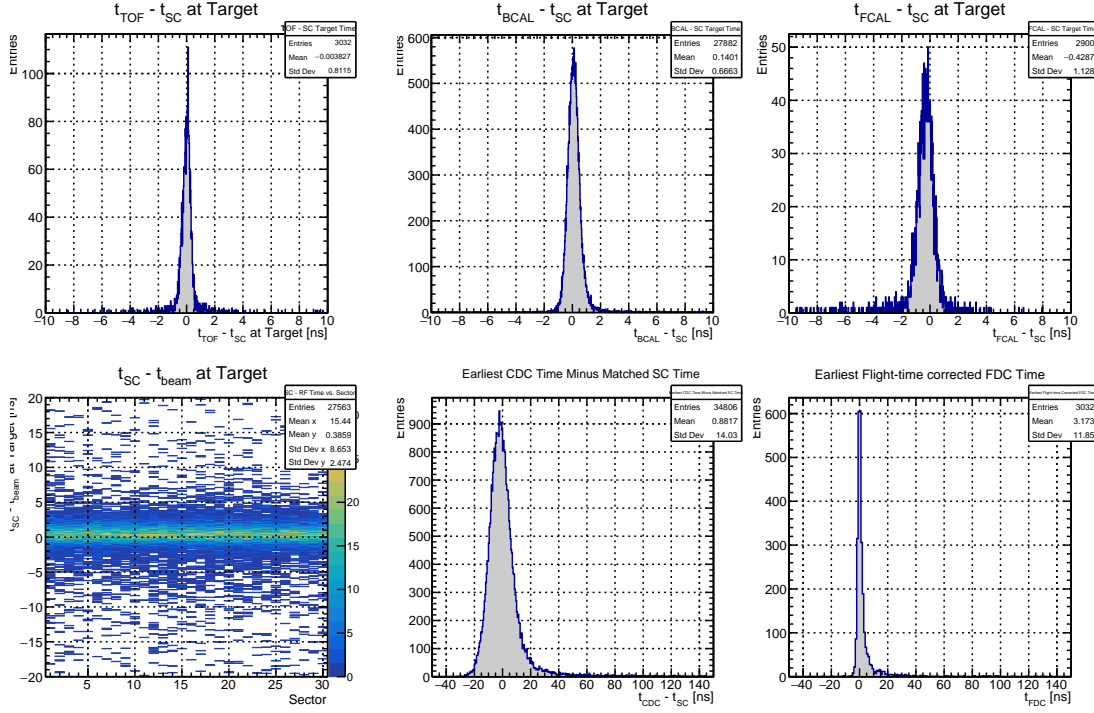
Figure 7: Illustration of timing calibration distributions for $K_L p \to K_S p$, $K_S \to \pi^+ \pi^-$ events.

various neutron induced reactions ($np \to np\pi^0$, $np \to d\pi^0\pi^0$, $np \to nn\pi^+\pi^0$, etc.). To perform calibration monitoring and possibly calibration itself, we have concentrated on a well-studied reaction with rather large cross sections, $np \to np\pi^0$, which can provide a sufficient number of neutral pions in a short time.

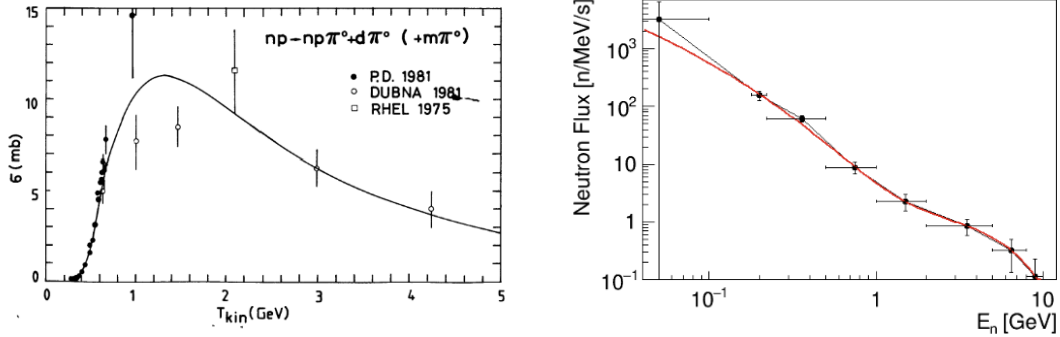Figure 8: Left: $np \to np\pi^0$ cross section. Right: neutron flux at cryogenic target.

We have evaluated π^0 yields from neutron-induced reactions, utilizing a standard KLF neutron flux and a $np \to np\pi^0$ cross section from [J. Bystricky, P. La France, F. Lehar, F. Perrot, T. Siemiarczuk, and P. Winternitz, J. Physique **48**, 1901 (1987)], see Fig. 8. From Ref. [P. Adlarson *et al.* Phys. Lett. B **774**, 599 (2017)], we know that this reaction is fully dominated by the isovector cross section, $I = 1$, so it is nearly identical to a reaction $pp \to pp\pi^0$, which we know better, including differential distributions and even polarization observables.

We get the following neutron-induced π^0 distribution. Total 140 π^0 events per second or 12M π^0 events

per day. This flux is expected to be not sufficient for a standard calorimeter calibration or a daily calibration that requires a minimum cluster energy threshold of 100 MeV, 1 GeV, 250 MeV in BCAL, ECAL and FCAL, respectively. Furthermore, for BCAL, the production vertex must be known within $\pm$ 2 cm which is not the case with a single track in the final state.

Taking into account neutron flux, cross section dependence, and reaction dynamics, photons originating from the reaction $np \rightarrow np\pi^0$ have the following distribution within the GlueX spectrometer. The result is shown for 1 day of running per 5 degree bin in polar angle and 10 MeV bin in photon energy. However, one can clearly see that all necessary angles are well populated, mostly with low-energy photons $E_\gamma \sim 100$ MeV, in line with the dominant photon energies of our hyperon program.
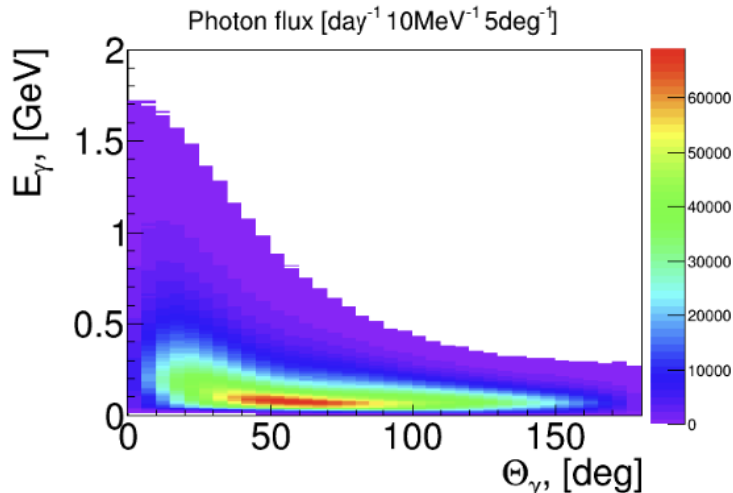

Figure 9: Photon flux from $np \rightarrow np\pi^0$ reaction for 1 day data collection per 5 degree and 10 MeV bins.

An initial calibration of the calorimeter gains and non-linearity corrections can be done with the few days of commissioning photon beam data that are planned to be collected, as described above. This data would be similar to that that is being collected by current GlueX running and would use the same calibration procedures. An illustration of the kinematics of photons from $\pi^0 \rightarrow \gamma\gamma$ decays from the photon beam data and the kinematics of photons from some representative K_L beam reactions is shown in Fig. 10. This shows that the calibration from the photon beam has good overlap with the photon kinematics for the KLF physics program. We note that the thresholds for the energy cells BCAL, ECAL and FCAL are 15 MeV, 25 MeV, and 150 MeV, respectively.

3.4 Particle Identification

Particle identification on the GlueX spectrometer is performed using the ionization energy deposited in the drift chambers and time-of-flight measurements using the Start Counter, forward TOF, and BCAL detectors. Examples of their performance as a function of the reconstructed particle momentum are given in Figs. 11 and 12. Generally, time-of-flight measurements are more effective for particle identification for tracks in the forward direction, due to precision ToF measurements and the long lever arm, while drift chamber dE/dx measurements are more effective for tracks at larger angles.

Since we are studying hadrons that include strangeness, many final states include K_S and Λ hadrons, which are well reconstructed in their decays $K_S \rightarrow \pi^+\pi^-$ and $\Lambda \rightarrow p\pi^-$, as illustrated in Fig. 13.

More detailed studies and the effect of reconstructing exclusive events are shown in the sections for individual reactions in Sec. 4.
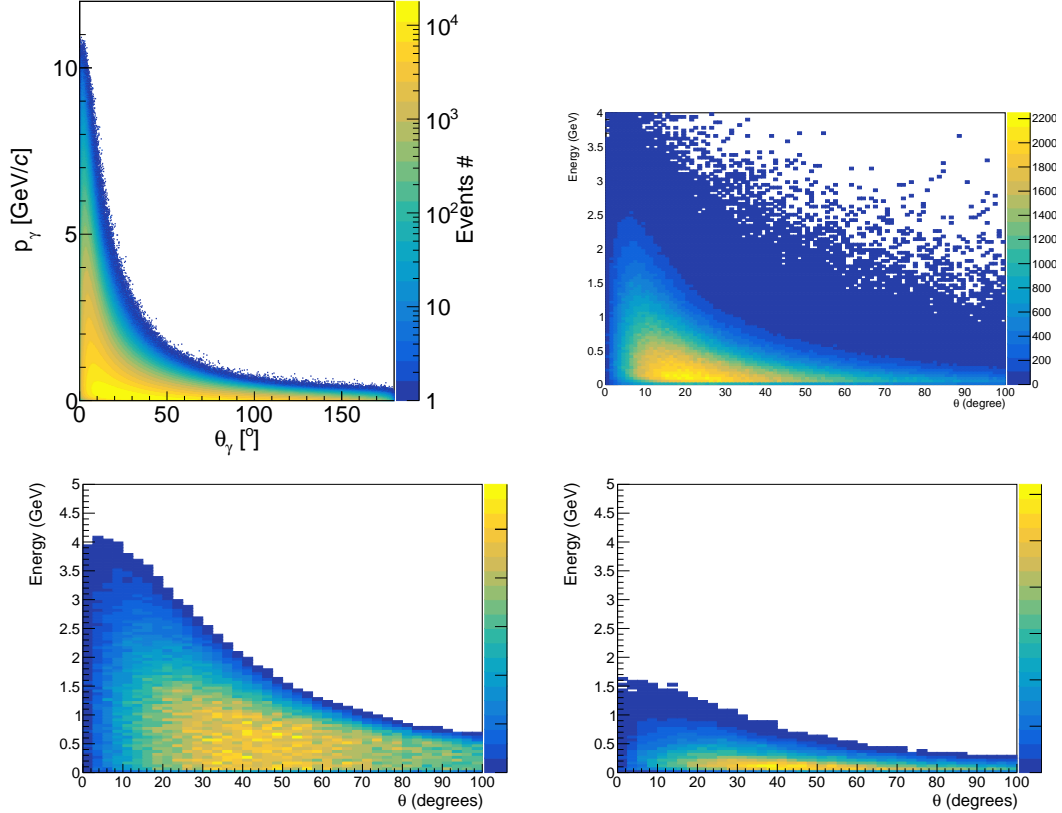
Figure 10: Simulated photon kinematics from $\pi^0 \to \gamma\gamma$ decays for various reactions: (top left) Generic γp interactions with the GlueX photon beam; (top right) $K_L p \to K^{*-}(892)\Delta^{++} \to (K^-\overline{\pi^0})\Delta^{++}$ with the t-exchange model described in Sec. 4.4; (bottom left) Phase space $K_L p \to \pi^0 \Sigma^+$ events with $W < 3$ GeV. (bottom right) $\Sigma^+ \to \pi^0 p$ decays from phase space $K_L p \to \pi^0 \Sigma^+$ events with $W < 3$ GeV.

3.5 Event Reconstruction in Spectrometer

The event reconstruction and analysis uses standard Hall D software with modifications for the reconstruction of the K_L beam. Charged particles and calorimeter showers are reconstructed with standard software, after which very loose particle identification selections are applied, and the final-state particles are combined and kinematically fitted to produce a set of ROOT analysis trees for a user-specified menu of reactions.

The primary addition to the reconstruction software is that for reconstructing the incident K_L beam momentum. The K_L beam momentum is calculated from the time-of-flight between the center of the KPT (approximately 24 m upstream of the cryotarget) and the primary vertex of a reconstructed reaction. The primary vertex is best determined by a kinematic fit to the reaction, where the resolution can be improved if multiple particles are generated from the primary vertex, and any displaced vertex from the decay of long-lived particles (*e.g.*, K_S and Λ) can be considered. The time of the primary vertex is determined by matching signals from subdetectors with good time resolution (TOF, BCAL, ST) to a charged particle track and propagating these times to the position of the primary vertex using the measured track momentum and path through the detector. The resolution of the K_L reconstruction will then depend on the reconstructed reaction, in particular on how many tracks are used to define the primary vertex, and the kinematics of the final-state particles themselves.

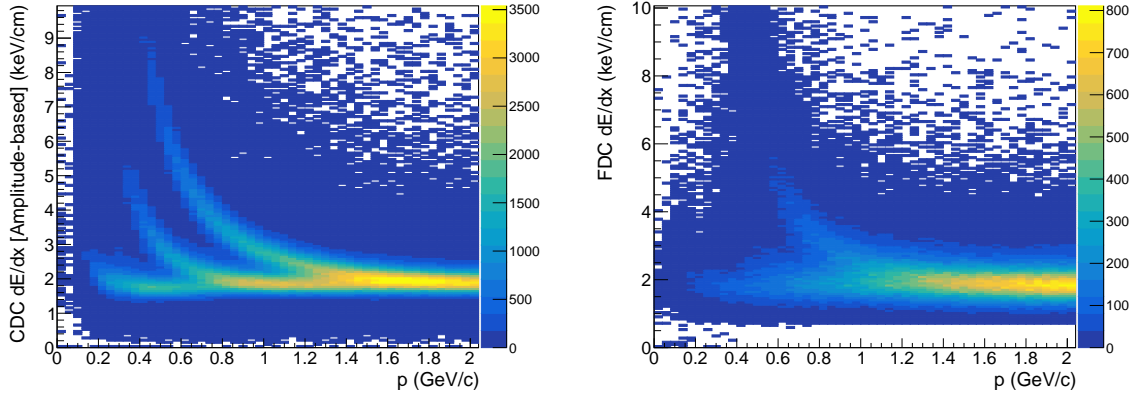To illustrate the general characteristics of the reconstruction of events induced by K_L, we simulated 1M

Figure 11: Energy deposited in the (left) CDC and (right) FDC as a function of particle momentum for hadrons simulated under KLF conditions. The different bands correspond to charged pion, kaons, and protons, going from bottom to top. All three particles are distinguishable at low enough momentum in the CDC, while only the pion and proton bands are apparent in the FDC.
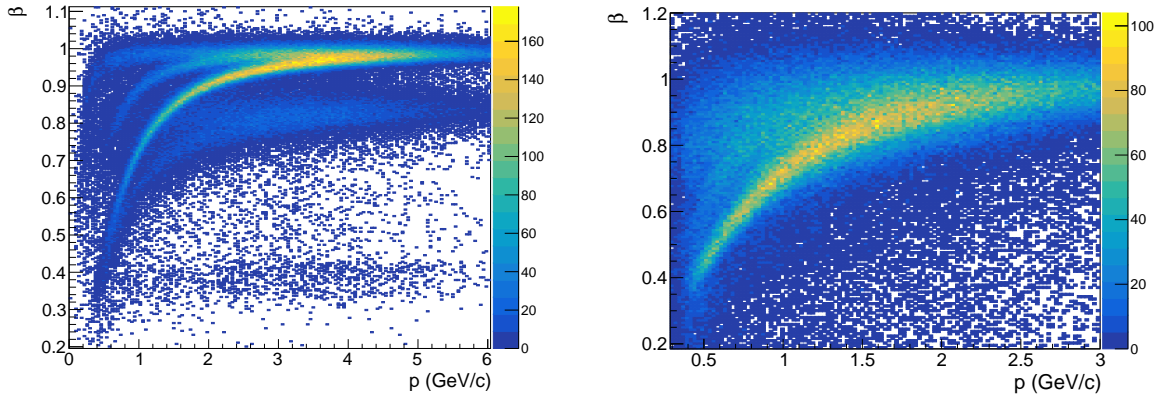

Figure 12: Reconstructed velocity as a function of particle momentum for charged particles in the (left) TOF and (right) BCAL detectors, for hadrons simulated under KLF conditions. The different bands correspond to charged pion, kaons, and protons, going from top to bottom.

$K_L p \to K_S p$ events with a flat K_L beam momentum distribution in the range $p(K_L) = 1 - 6$ GeV, and reconstructed K_S in its decay $K_S \to \pi^+\pi^-$. Several aspects of the event reconstruction are illustrated in Fig. 14, and the reconstructed K_L momentum and final-state invariant mass resolutions are shown in Fig. 15.

More detailed studies for individual reactions are given in Sec. 4.

3.6   Flux Monitor Calibration

The Flux Monitor consists of 3 independent detector systems: detector start, detector stop, and tracker; see FM MEMO [M. Bashkanov, D. P. Watts, N. Zachariou, E. Chudakov, M. Amaryan, J. Ritman, J. Stevens, I. Strakovsky, *Flux Monitor Notes*, GlueX-doc-3603]. A start detector has a two-layer design with the second layer turned by half an element relative to the first layer. This arrangement allows to perform a calibration of the start detector with any charged tracks regardless of their origin angular and momentum distributions. A similar calibration arrangement is performed for the Stop Detector. Each element has a double-side readout,
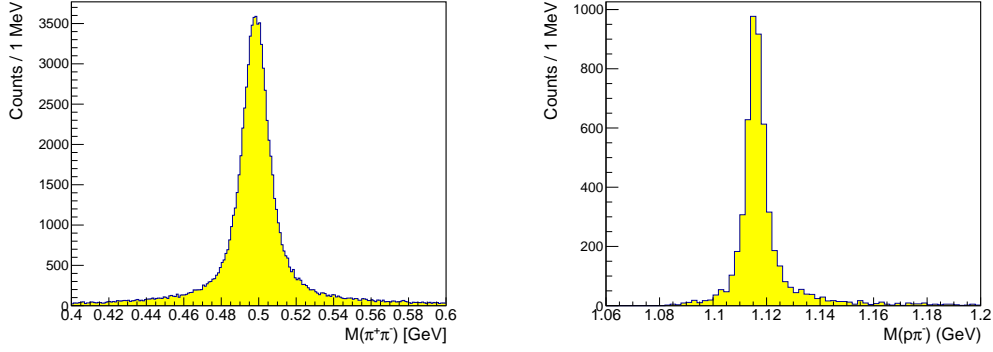
Figure 13: Reconstructed mass peaks for (left) $K_S \to \pi^+\pi^-$ decays for simulated $K_L p \to K_S p$, $K_S \to \pi^+\pi^-$ events, and (right) $\Lambda \to p\pi^-$ decays for simulated $K_L p \to \Lambda\pi^+$, $\Lambda \to p\pi^-$ events.
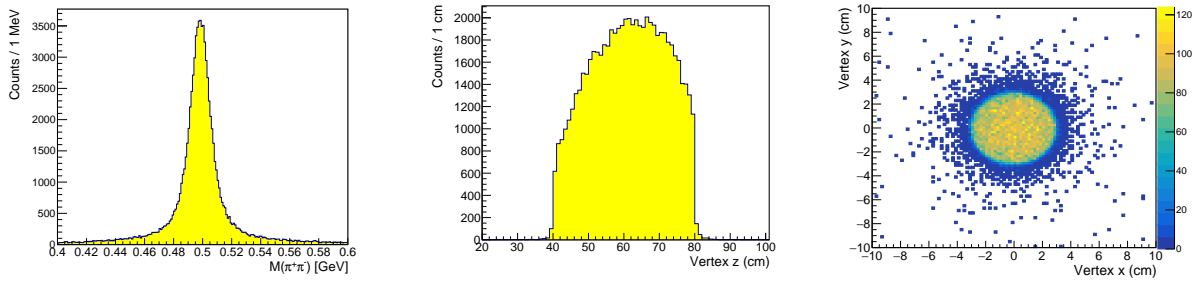

Figure 14: Distributions for reconstructed $K_L p \to K_S p$, $K_S \to \pi^+\pi^-$ events: (left) $\pi^+\pi^-$ invariant mass showing a clear peak for $K_S \to \pi^+\pi^-$ decays; (middle) primary vertex z-position, showing that the events are well-reconstructed within the target length of $z = 40 - 80$ cm; (right) primary vertex xy-position, show that the events are well-reconstructed within the target radius of 3 cm.
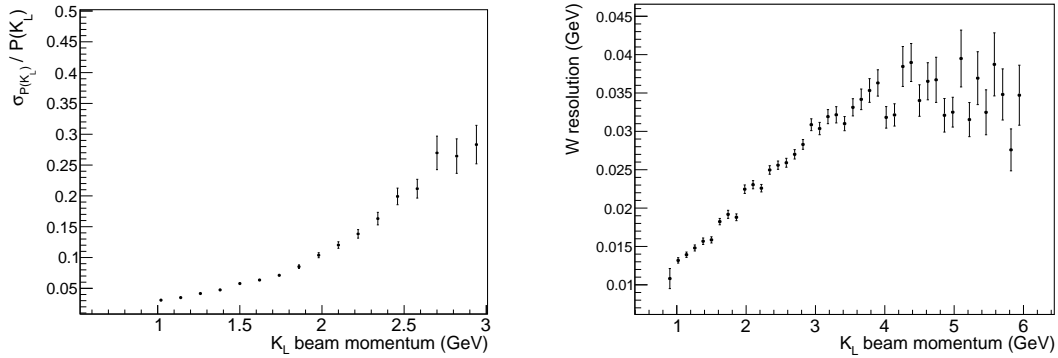

Figure 15: Resolutions for reconstructed $K_L p \to K_S p$, $K_S \to \pi^+\pi^-$ events: (left) incident K_L momentum resolution as a fraction of K_L momentum; (right) final state W invariant mass resolution.

but in addition to a wall of vertical bar elements, there are two horizontal calibration bars to align the timing of all of the bars consistently. The calibration of a tracker is performed relative to a Start detector. More details on KLF calibration / reconstruction procedures can be found in the FM MEMO [M. Bashkanov,
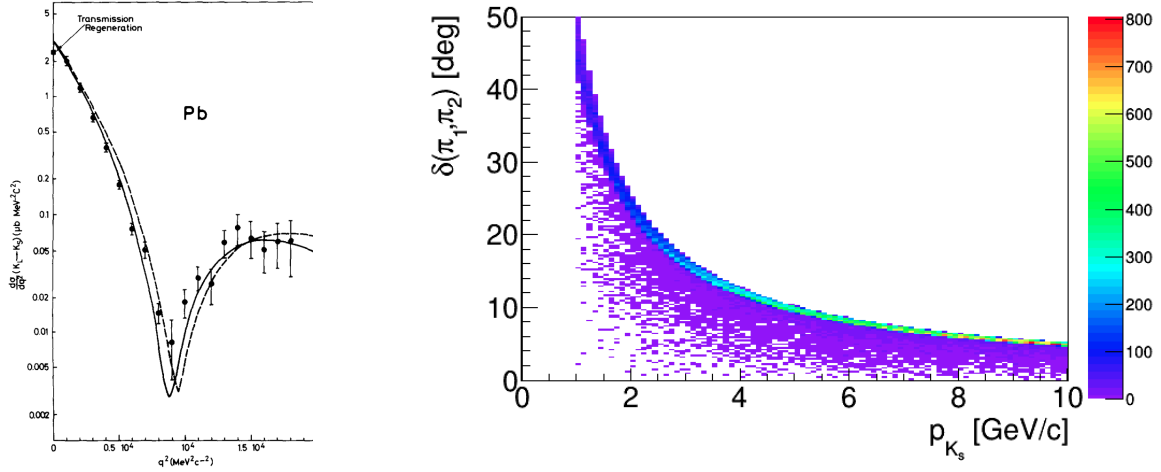
16

D. P. Watts, N. Zachariou, E. Chudakov, M. Amaryan, J. Ritman, J. Stevens, I. Strakovsky, *Flux Monitor Notes*, GlueX-doc-3603].

Figure 16: $K_L - K_S$ regeneration cross section as a function t from Ref. [H. Foeth *et al.* Phys. Lett. B **31**, 544 (1970)] (left) and $\pi^+\pi^-$ opening angle as a function of kaon momentum (right).

The only nontrivial calibration we need to perform with the Flux Monitor is an absolute adjustment of timings relative to beam bunches. To do it, we will insert a 1 mm tungsten foil in a beam line, right after the pair-spectrometer magnet. A beam K_L undergoes regeneration $K_L - K_S$ in tungsten. This process is carried out coherently on nuclei, leading to a very large $\sigma \sim A^2$ cross section and a small angular range - the opening angle $\delta_{K_L-K_S} << 1$ deg, Fig. 16 (left). We can safely assume that all newly coherently produced K_S have the same direction as the initial K_L.

Because the tungsten foil is thin, the z position of the regeneration process is known very well, allowing cross-check and cross-verification of the tracker calibration. The momentum of the outgoing K_S is equal to the momentum of the incoming K_L. However, the main K_S decay channel, $K_S \rightarrow \pi^+\pi^-$ has a direct relation between the opening angle of the pions and the momenta K_S, see Fig. 16 (right). Hence, one can reconstruct K_S momenta in two independent ways - with angles and with time-of-flight, allowing precise time alignment of all FM detectors. The K_S regeneration method also allows an independent verification of the kaon flux, leading to a reduction of the systematic uncertainty of our main K_L-in-flight decay flux determination method. The thickness of a tungsten foil is chosen to produce ~ 1 K_S per second. Running 1 day with tungsten foil is expected to be sufficient to perform precise FM detector time adjustments. The tungsten foil can be removed or inserted remotely allowing for additional cross-verification whenever it is necessary.

An insertion of tungsten foil would not massively change the rate of events in the Flux Monitor. If we did not impose any cuts, then a 2 charged track rate from in-flight K_L decays would be 25 times higher than from K_S. However, a simple 5 degree coplanarity cut reduces this ratio to 1:1, and an additional vertex cut can improve it further by a factor of ~ 30, making the extraction of coherent K_S events pretty straightforward.

4 Key Analysis Channels

Details of analyses for key channels ($K_L p \to \pi^+ \Lambda$. $K_L p \to K^+ \Xi^0$ ($\Xi^0 \to \pi^0 \Lambda$), $K_L p \to K_S p$ ($K_S \to \pi^+ \pi^-$), $K_L p \to K^+ n$, and $K_L p \to K^*(892)p \to K^+ \pi^- p$) are given in the following subsections.

4.1 $K_L p \to \pi^+ \Lambda$

As our objective is to further the knowledge of hyperons and the interactions of strange particles, strange resonances are a natural aspect of our studies. Strange resonances are excitations in a hyperon, denoted Λ^*, Ξ^*, and Σ^*, representing resonances with isospin 0, 1/2, and 1, respectively. These states are analogous to the N^* and Δ^* resonances. Based on the fact that there are 17 N^* states and 10 Δ^* states, we would expect that there are at least 27 Σ^* states, but only 12 have been experimentally discovered so far [M. Amaryan *et al.* arXiv:2008.08215 [nucl-ex]].

Many charged-kaon scattering experiments have provided data, along with some neutral-kaon scattering data from SLAC. SLAC performed a neutral-kaon on proton scattering experiment yielding 2512 Λs and 1065 Σ^0s [R. J. Yamartino *et al.* Phys. Rev. D **10**, 9 (1974)]. However, the current amount of neutral-kaon data is not sufficient to reveal these missing hyperon resonances. The KLong Facility, after 100 days of operation, is expected to provide more than three orders of magnitude more Σ and Λ data than SLAC. A study of BnGa partial wave analysis (PWA) revealed that these data could reveal the existence of three of these hidden resonances due to the significant increase in the production cross section of the hyperons and the different polarization observables seen [M. Amaryan *et al.* arXiv:2008.08215 [nucl-ex]]. Lastly, the parity violating decay of Λ allows its polarization to be measured, which provides a strong constraint for PWA [M. Bashkanov, N. Zachariou, K. Park, S. Taylor, and I. Strakovsky, *KLF Analysis Report: Hyperon Spectroscopy Simulation Studies*, KLF Note, 2020].

4.1.1 Λ Analysis Specifications

The Λ baryon is an isospin 0 particle with a mass of 1115.7 GeV that contains an up, down, and a strange quark. The Feynman diagrams for the production of Λs by neutral-kaon scattering are shown in Fig. 17.
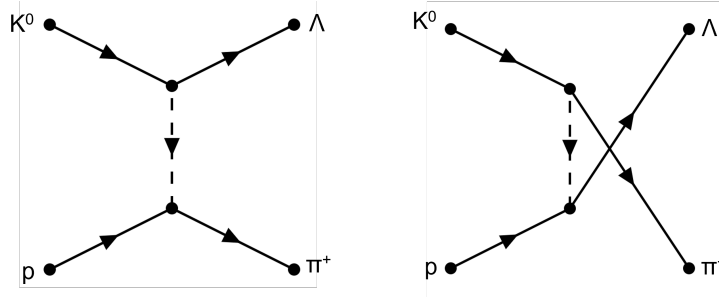

Figure 17: Depiction of the t-channel and u-channel Feynman diagrams of the production of Λ baryons from neutral-kaon scattering. The t channel process is shown in <u>left</u> and the u channel process is shown on the right.

The Λ possesses two main decay channels as shown below

$$\Lambda \longrightarrow \pi^- + p \tag{1}$$

and

$$\Lambda \longrightarrow \pi^0 + n , \tag{2}$$

which have branching ratios of 63.9% and 35.8%, respectively [P. A. Zyla *et al.* [Particle Data Group], Prog. Theor. Exp. Phys. **2020**, 083C01 (2020)]. For this analysis, only the charged channel was studied.

Associated with the Λ channel are two background channels, namely the Σ^0 and the Ξ^0 decays,

$$\bar{K}^0 + p \longrightarrow \pi^+ + \Sigma^0 \,,$$
$$\Sigma^0 \longrightarrow \gamma + \Lambda \,, \tag{3}$$

and

$$\bar{K}^0 + p \longrightarrow K^+ + \Xi^0 \,,$$
$$\Xi^0 \longrightarrow \pi^0 + \Lambda \,, \tag{4}$$

which also produce Λs. There is also a tertiary background, the K_s production,

$$K_L + p \longrightarrow p + K_s \,,$$
$$K_s \longrightarrow \pi^+ + \pi^- \,, \tag{5}$$

which has the same detected particles, the proton and the charged pions, as the Λ signal channel. When looking at the resulting distributions, only a negligible number of events have the requisite $m_{p\pi^-}$ invariant mass to mimic the signal, so further analysis of this background was excluded.

For this analysis, 1M events were generated for each of the channels described above with a KLong particle generator that utilized a realistic neutral-kaon beam momentum profile. The beam was generated with an energy range of $0.5 - 6$ GeV and only events with $W < 3$ GeV were analyzed. The simulation used Geant4 to simulate particle interactions with the KLF upgraded GlueX geometry, and reconstruction was performed with JANA.

4.1.2 Reconstruction

In order to reconstruct the Λs, we need to measure the incoming beam and detect the decay particles from the interaction of the beam and the target. The beam energy for this analysis channel has been reconstructed and has an energy resolution between 0.14 and 0.6 GeV, depending on the beam energy, as outlined in Fig. 18. In addition to the general trend of increasing the width with the energy of the beam, Fig. 18 also illustrates that the mean of the distributions increases with energy.

To detect the decay particles of the neutral-kaon scattering, we need to measure the energy deposited in the calorimeters. The total energy deposited for the detected proton, π^+, and π^- in the three calorimeters, *i.e.*, the Preshower Barrel Calorimeter (BCAL), BCAL, and Forward Calorimeter (FCAL), as a function of incident beam energy, is illustrated in Fig. 19. The plots demonstrate that the deposited energy does not strongly depend on the beam energy and that the majority of the deposited energy, regardless of particle type, is around 0.5 GeV.

In addition to the energy deposited in the calorimeters, particle identification can be made by the energy that the charged particles lose in a drift chamber. Here, the energy loss in the Central Drift Chamber (CDC) is represented as the energy loss per centimeter of the CDC (dE/dx). Fig. 20 shows this energy loss in the CDC for the proton, π^+, and π^- as a function of the reconstructed momentum of the particles. The images show that the proton and the π^+ are well separated at low energy.

Lastly, using the full reconstruction software, the kinematics of the proton and charged pions can be reconstructed, allowing the Λ to be reconstructed. Fig. 21 shows the reconstructed momentum and polar angle (θ) of the detected particles. From the figures, one can see that the π^- momentum is mainly below 1 GeV and does not strongly depend on θ. The proton and the π^+ have a more linear relationship between the momentum and polar angle.

4.1.3 Event Selection

To properly study $\pi^+\Lambda$ production, we have to deal with the background of $\pi^+\Sigma^0$ and $K^+\Xi^0$. Since background channels possess more particles detected than the signal, γ, π^+, π^-, and the proton for the Σ^0
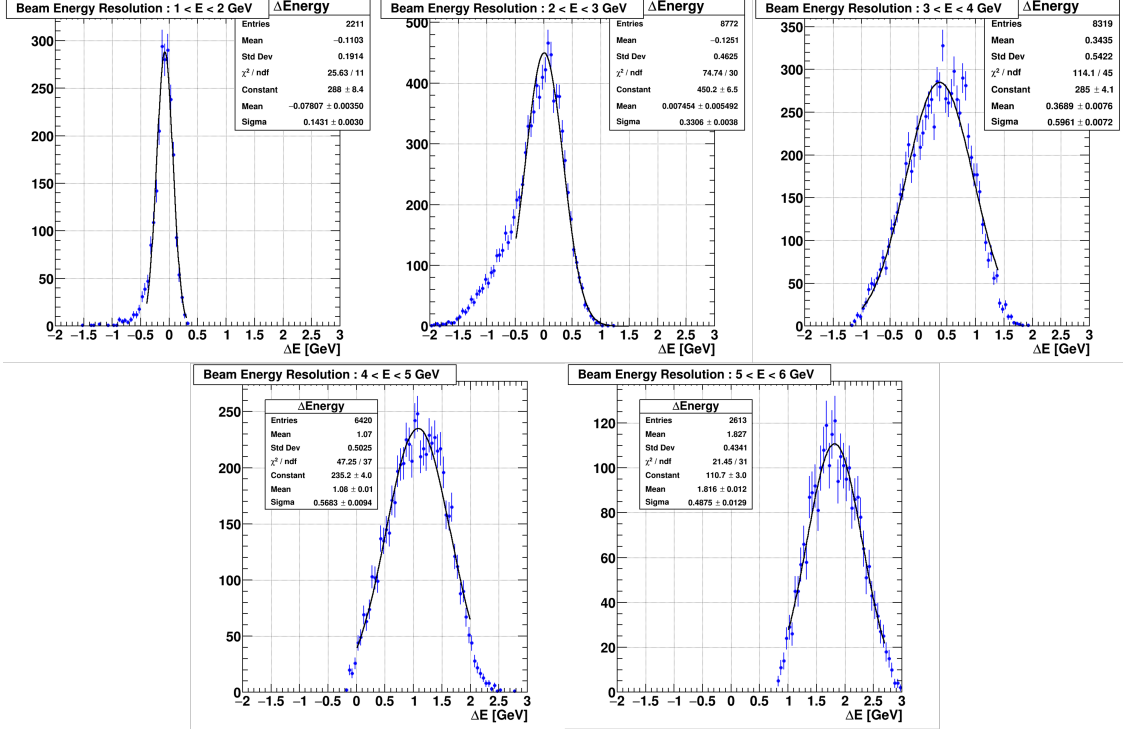
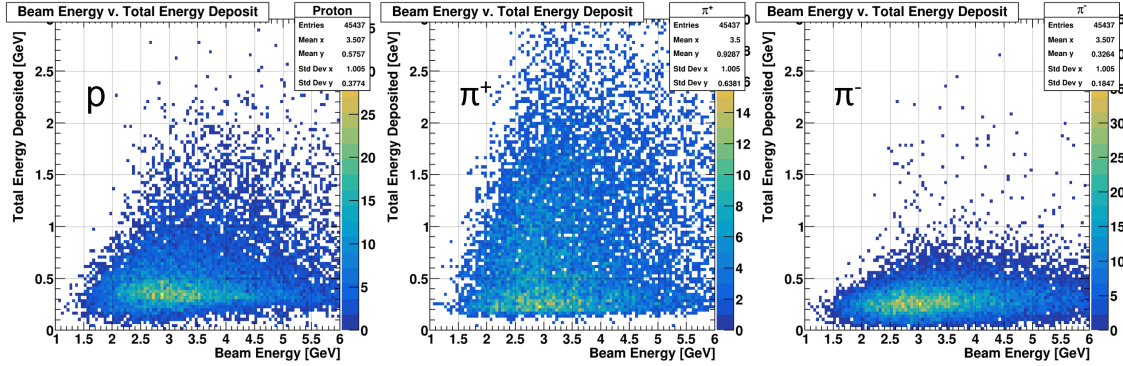Figure 18: Beam energy resolution as a function of beam energy.

Figure 19: Total calorimeter energy deposited as a function of beam energy for the proton, π^+, and π^- plotted to the <u>left</u>, <u>middle</u>, and <u>right</u>, respectively.

channel and K^+, 2γs, π^-, and the proton for the Ξ^0 channel versus π^+, π^-, and the proton for the signal, the kinematics of the state X is a natural choice for signal-background discrimination. For this channel, the X-state is the remnant of the beam-target system when the detected particles are subtracted, *i.e.*,

$$X := \bar{K}^0 + p - \Lambda - \pi^+ , \tag{6}$$

with the Λ being reconstructed from the detected proton and π^-. For this analysis, K^+ from the Ξ^0 channel was treated as a misidentified π^+. From studying the signal and background X-state kinematics, a series of selection cuts were developed :
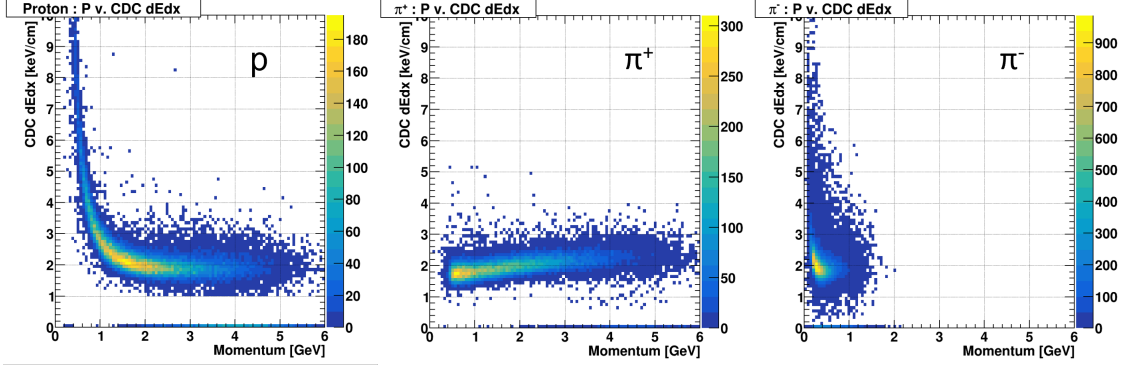
Figure 20: Energy loss per centimeter in the CDC as a function of particle momentum for the proton, π^+, and π^- plotted to the <u>left</u>, <u>middle</u>, and <u>right</u>, respectively.
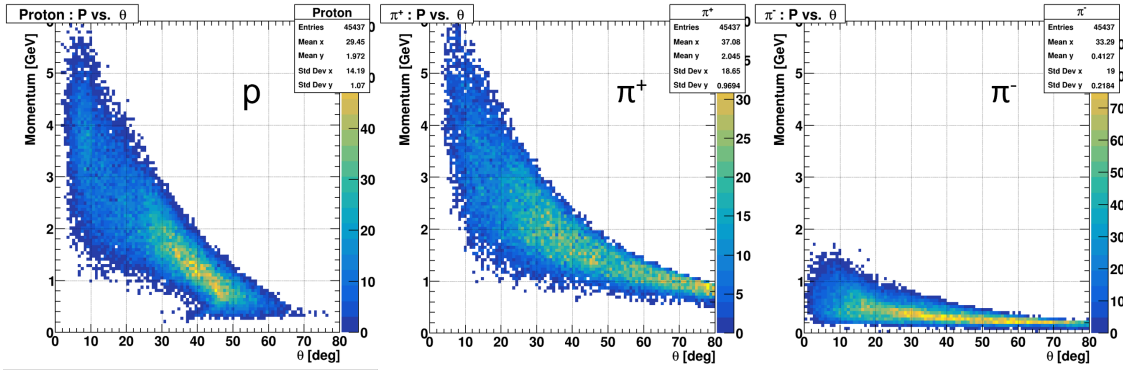

Figure 21: Momentum vs. polar angle plots for the proton, π^+, and π^- plotted to the <u>left</u>, <u>middle</u>, and <u>right</u>, respectively.

- $M_x < 0$ GeV (M_x is the mass for the X-state).

- $M_{xt}^2 < 0.081$ GeV^2 (M_{xt}^2 is the transverse mass of the X-state, with $M_{xt}^2 = E_{xt}^2 - p_z^2$).

- $|p_{xx}| < 0.094$ GeV/c (p_{xx} is the momentum of the x direction of the X state).

- $|p_{xy}| < 0.094$ GeV/c (p_{xy} is the momentum of the y direction of the X state).

Fig. 22 shows the first two selection cuts, with the events passing the cuts being to the left and bottom of the red line. From the figure, it is clear that the background channels have events outside the cut, whereas the signal remains largely uncut. The second sets of cuts, relating to the transverse momenta of the X state, are shown in Fig. 23. Here, like in the first sets of cuts, the background channels have a larger fraction of events outside the red cut line because the X-state transverse momenta are more strongly peaked near zero for signal as opposed to the backgrounds.

The effects these selection constraints have on the invariant mass of the $\pi^- p$ for the signal and background channels can be seen in Fig. 24, the upper row showing the invariant mass distributions *sans* selection cuts and the lower row showing the distributions with cuts. Within each set of plots, the invariant mass distributions have been fit with a double Gaussian. The signal Gaussian is colored green, the background Gaussian is colored orange, and the combined fit is colored red. From the resulting graphs it can be seen that this level of constraints only removes about 10% of the signal distribution, but more than 50% of the background Σ^0s and almost 90% of the background Ξ^0s.
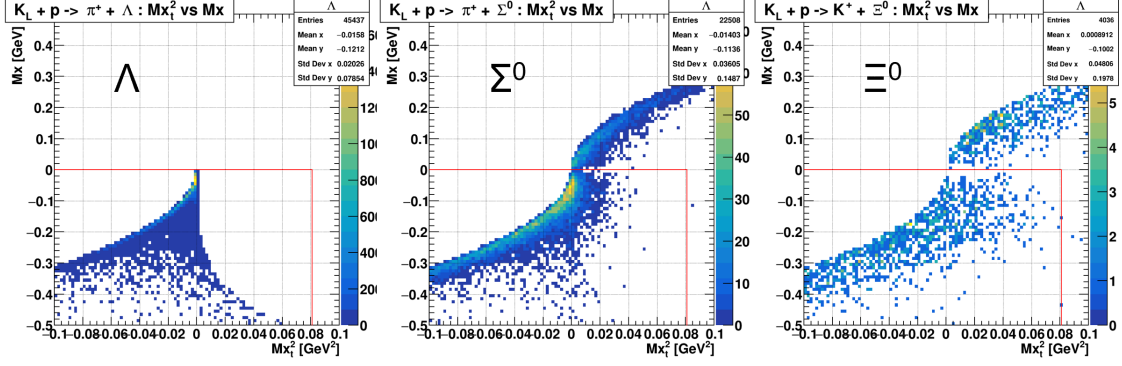
21

Figure 22: Transverse X-state mass squared vs. X-state mass for the Λ, Σ^0, and Ξ^0 channels plotted to the left, middle, and right, respectively. The red lines denote the selection cut boundaries.

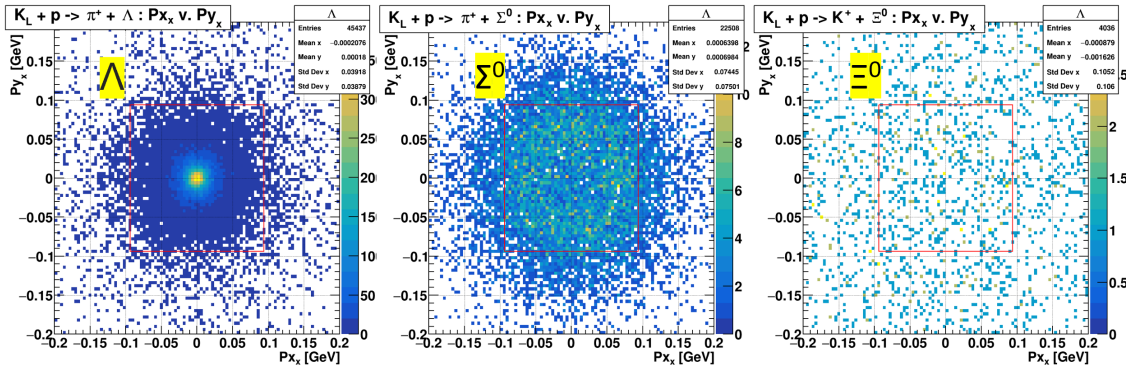Figure 23: X-state x-direction momentum vs. y-direction momentum for the Λ, Σ^0, and Ξ^0 channels plotted to the left, middle, and right, respectively. The red box demarcates the selection cut boundary.

Rounding out this section are the particle efficiencies shown in Fig. 25 and Fig. 26. The first figure illustrates the Λ momentum and polar angle efficiencies of the Λ, Σ^0, and Ξ^0 channels. The momentum distributions show that the efficiency is flat for the background channels, but has some enhancement at low momentum for the signal channel. The polar angle distributions show that the efficiencies are flat for the Λ channel and the Ξ^0 channel, but reveal some enhancement of the Σ^0 channel at low θ. The second figure shows the beam energy efficiencies of the channels and the efficiency of $cos(\theta_{cm})$. $cos(\theta_{cm})$ is the cosine of the polar angle of the reconstructed Λ in the $\bar{K}^0 p$ center of mass frame. The beam energy efficiencies for all channels show an increase in efficiency until about 1.5 GeV, and then a decrease as the beam energy increases. The $cos(\theta_{cm})$ efficiencies of the three channels are flat between -0.8 and 0.75 and then increase in efficiency to approximately 0.9.

4.1.4 Λ Yield

The invariant mass $\pi^- p$ as a function of the incident beam energy with associated double Gaussian fit is shown in Fig. 27. The graphs show that the Λ mass is well reconstructed, since the mean extracted from the graphs is within a fraction of a MeV of the accepted Λ mass and the extracted width is around 3 MeV, regardless of the beam energy bin. Lastly, the number of Λ baryons as a function of beam energy was extracted from the fits shown in Fig. 27 using the integral of the signal Gaussian and the error was calculated using the fit covariance matrix. The results are plotted in Fig. 28, illustrating a significant increase in the number of Λ s from the beam energy bin $1 - 2$ GeV to the bin $2 - 3$ GeV, and a slow decrease as the energy
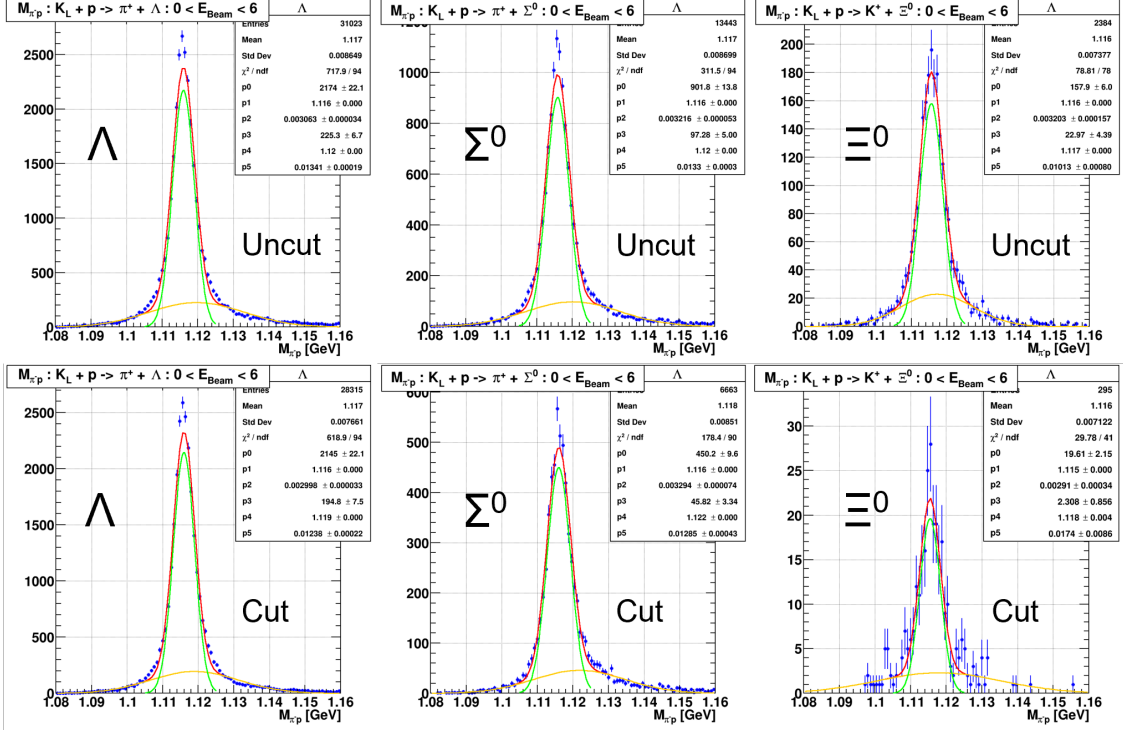
Figure 24: $\pi^- p$ invariant mass distributions with a double Gaussian fit for the Λ, Σ^0, and Ξ^0 channels plotted in the left, middle, and right columns, respectively. The top row shows the channels without any of the section cuts, and the bottom row shows the distributions after the selection cuts have been made. The Gaussian signal, Gaussian background, and total fit are depicted in green, orange, and red, respectively.

bin increases.

4.1.5 Summation

In conclusion, the $\pi^+\Lambda$ channel has been studied together with its associated background channels. The beam energy has been resolved to within $0.14-0.6$ GeV depending on the incident beam energy, with higher energies having less resolution. Using energy deposits in calorimeters and measurements of dE/dx in the CDC, π^+ and particles from decay of Λ can be identified. Using the transverse kinematic variables of the state X, selection cuts were developed that removed more than 50% of the background Σ^0 and almost 90% of the background Ξ^0, while leaving more than 90% of the signal $\pi^+\Lambda$. The efficiency distributions have shown increases near low momentum and low polar angle, but a flat $cos(\theta_{cm})$ distribution and a decreasing efficiency as the beam energy increases. Lastly, the invariant mass $\pi^- p$ has been plotted as a function of the beam energy and the number Λs in this analysis sample has been extracted.
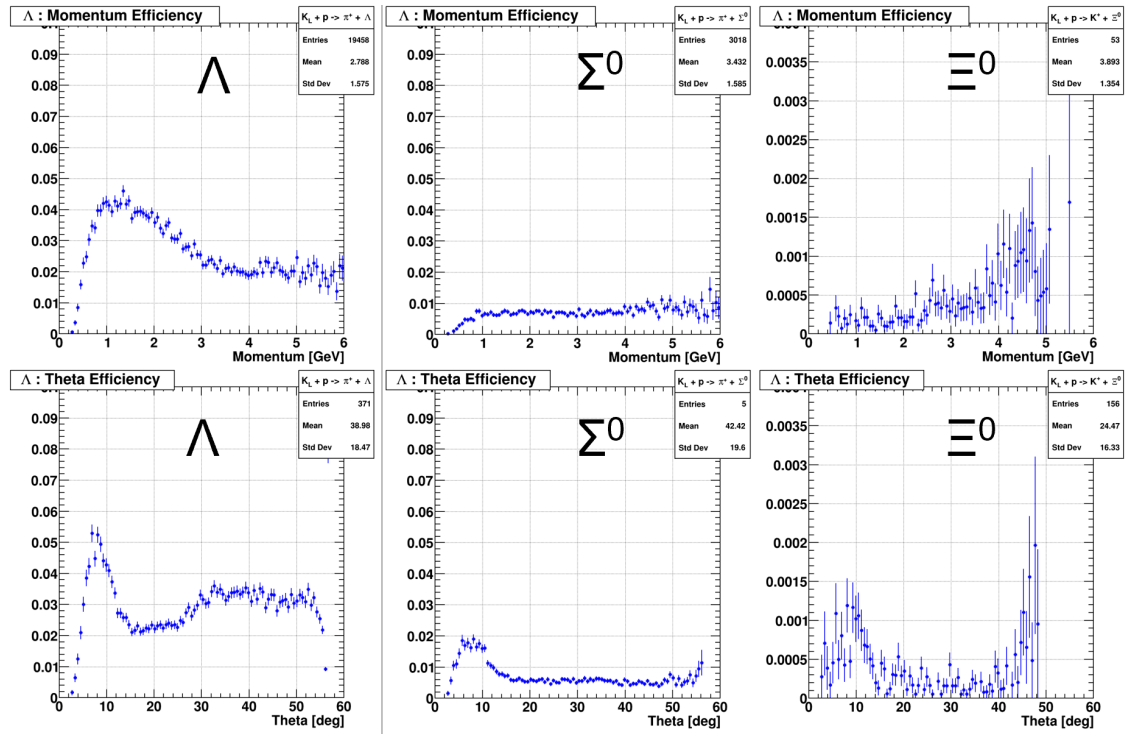
Figure 25: Λ momentum and polar angle efficiency distributions for the Λ, Σ^0, and Ξ^0 channels plotted in the left, middle, and right columns, respectively. The top row shows the momentum efficiencies and the bottom row shows the polar angle efficiencies.
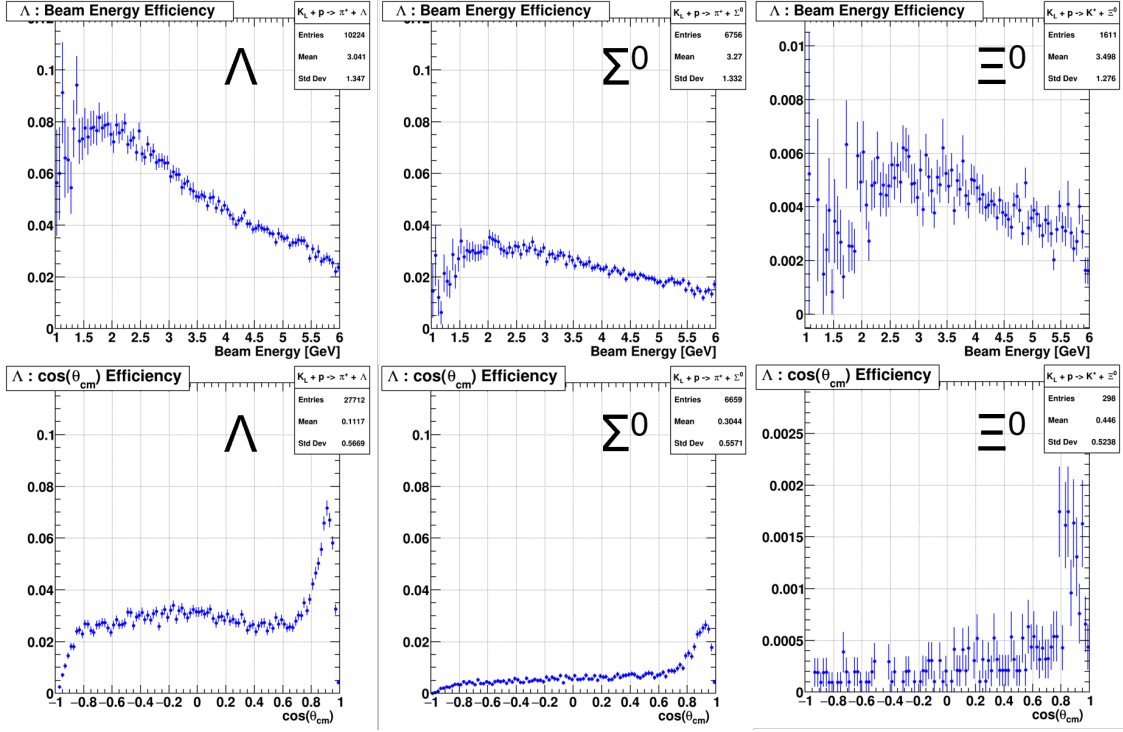
Figure 26: Λ beam energy and $cos(\theta_{cm})$ efficiency distributions for the Λ, Σ^0, and Ξ^0 channels plotted in the left, middle, and right columns, respectively. The top row shows the beam energy efficiencies and the bottom row shows the $cos(\theta_{cm})$ efficiencies.
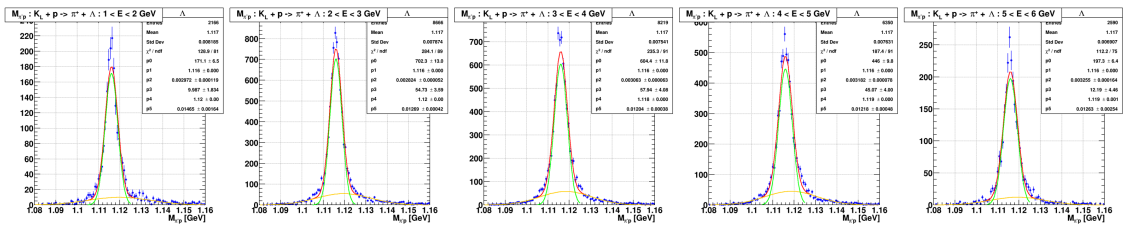

Figure 27: $\pi^- p$ invariant mass distributions of the $\pi^+\Lambda$ channel as a function of beam energy. The Gaussian signal, Gaussian background, and total fit are depicted in green, orange, and red, respectively.
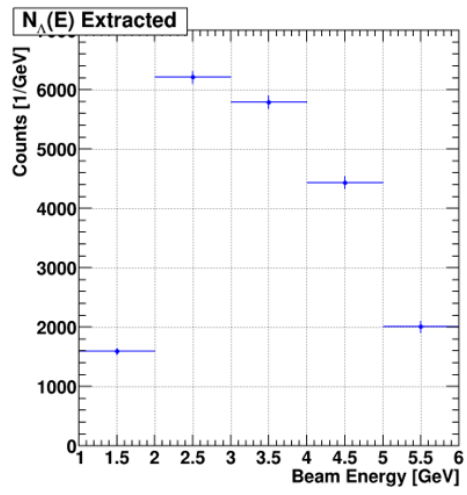
Figure 28: Extracted Λ yield with associated error from the signal channel as a function of beam energy.

4.2 $K_L p \to K^+ \Xi^0 \quad (\Xi^0 \to \pi^0 \Lambda)$

Studying cascade data will allow constraints to be placed on dynamical coupled-channel models and identify resonances that do not couple strongly to $\pi\Lambda$ but instead decay preferably to $K\Xi$; this is analogous to resonances N^* that do not couple strongly to πN but are cleanly seen in $K\Lambda$ and $K\Sigma$ channels. In addition, cascade data on proton and neutron targets will allow the measurement of missing excited states Ξ^* and determination of their properties. For example, although they have been experimentally established, many properties of $\Xi(1690)$ and $\Xi(1820)$ remain unknown. States like these can be easily identified and isolated in KLF using missing-mass and invariant-mass techniques, with further analysis to measure their quantum numbers.

With regard to non-resonant contributions that could interfere with hyperon production amplitudes and distort their signals, the reaction $K_L p \to K^+ n$ is able to provide a clean and controlled way to study and eliminate non-resonant contributions, as the formation of intermediate resonances in this reaction is forbidden.

The $K_L p \to K^+ n$ reaction also serves as the background to the $K_L p \to K^+\Xi$ reaction, since both channels have a kaon in the final state. Up to $W = 2.3$ GeV/c these channels can be well separated by just a missing mass. At higher W, one can either use background subtraction techniques or use an exclusivity condition with detection of Ξ^0 decay products to completely eliminate the neutron background. Here we will only concentrate on fully exclusively reconstructed $K_L p \to K^+\Xi^0$ events.

4.2.1 Generator

The generator employed, `KLGenerator_hddm_V3`, is capable of describing a comprehensive range of K_L reactions on both proton and neutron targets. The generator is also capable of generating events from γp and np events, which will be useful for beam-related background studies.

For the work presented, the generator has been configured to produce events from the $K_L p \to \Xi^0 K^+$ channel, sampling a K_L beam energy spectrum in the 1.0 to 4.0 GeV energy range (corresponding to a $W < 3$ GeV/c range of interest for hyperon studies). 10M events were generated for the study presented.

4.2.2 Reconstruction

Generated events were processed through the Hall D software, with Ξ^0 and subsequent daughter decays (Λ^0 and π^0) handled by GEANT4, which also handles detector smearing effects.

The HDDM (Hall D Data Model) files produced by the generation and smearing steps are passed through a *ReactionFilter*, used in the Hall D software stack to generate ROOT trees for analysis in a DSelector; a Hall D implementation of the standard TSelector class in ROOT.

The DSelector automatically performs some loose particle ID selections and combinatorics for the final state, and can implement a kinematic fit. The results for this channel are shown for a constrained kinematic fit of the vertex and the 4 momentum, without mass restrictions on Ξ^0.

4.2.3 Particle Identification

Three topologies can be used to reconstruct the reaction $K_L p \to K^+\Xi^0$ on free proton targets. Topology 1 requires the detection of a K^+, Topology 2 requires the detection of a K^+ and a Λ using its high branching ratio to a pair $\pi^- p$ (63.9%), and Topology 3 requires the detection of all particles in the final state, including the decay of two photos of $\pi^0 \to \gamma\gamma$. Here we will only concentrate on fully reconstructed final state events, Topology 3, *e.g.*, $K_L p \to K^+\Xi^0 \to K^+\Lambda\pi^0 \to K^+ p\pi^-\gamma\gamma$.

Figure 29 shows the identification of the charged track within the GlueX spectrometer for charged final-state particles (K^+, p, π^-) in reaction $K_L p \to K^+\Xi^0$. This is performed by momentum-dependent selection on the $\frac{dE}{dX}$ distributions in the drift chambers (CDC). For more details on GlueX PID, see Sec. 3.4. Neutral particles are identified by deposition of energy in calorimeters (BCAL and FCAL), with π^0 identified from the summed 4-momentum of energy deposits consistent with two final-state photons.

The distributions of the polar angle *vs.* momentum distributions are shown in Figure 30.
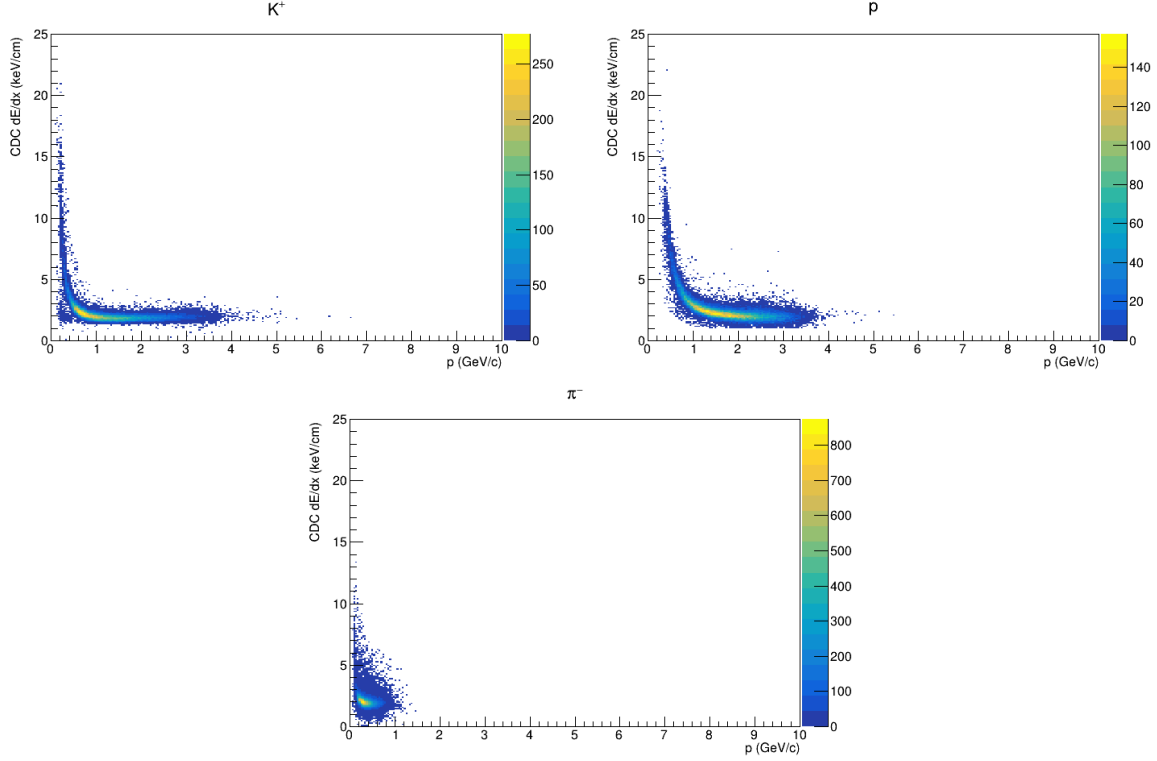
Figure 29: dE/dX vs momentum for K^+ (top-left), p (top-right), and π^- (bottom).

4.2.4 Ξ^0 Analysis

With the final-state particles established, Ξ can be reconstructed from its daughter decays. First, π^0 is reconstructed by means of the invariant mass of two photos. This is shown in Figure 31 (left).

The Λ^0 is reconstructed from its charged decay to $p\pi^-$, which has a branching fraction of 63.9%. The invariant mass of this is shown in Figure 31(middle). The complete reconstructed Ξ^0 invariant mass is shown in the Figure 31 (right).

To further refine event selection and reduce background, subsequent cuts are made on the overall missing mass of the final state system, M_X, eliminating events outside the mass range $-0.03 \to 0.02$ GeV^2. Additional cuts are applied to the invariant mass of the intermediate π^0 and Λ^0 ($0.1 < M_\pi < 0.17$ GeV, and $1.1 < M_\Lambda < 1.15$ GeV, respectively).

The missing squares of the mass of all final state particles (cut is applied from $-0.3 < M_X < 0.2$ GeV^2) are shown in Figure 32 (left).

The final invariant mass distribution Ξ^0 after all cuts is shown in Figure 32 (right).

In case of exclusive Ξ^0 detection, Topology 3, the reaction $K_L p \to K^+ \Xi^0$ can be reconstructed extremely well in a manner that is essentially background-free. As expected, the detection efficiency is highest for Topology 1 (including detection of K^+) reaching a maximum at 60 % for $W = 2.05$ GeV. The efficiency for Topology 3, where all particles are detected, is much smaller, about $\sim 1\%$ only.

In 100 days of beamtime, we expect 3×10^6 $K_L p \to K^+ \Xi^0$ events to occur in the cryogenic target. Of these, one can reconstruct 2×10^6 events for Topology 1 ($K_L p \to K^+ X$); and 2×10^4 for Topology 3 (fully exclusive $K_L p \to K^+ \Xi^0$).

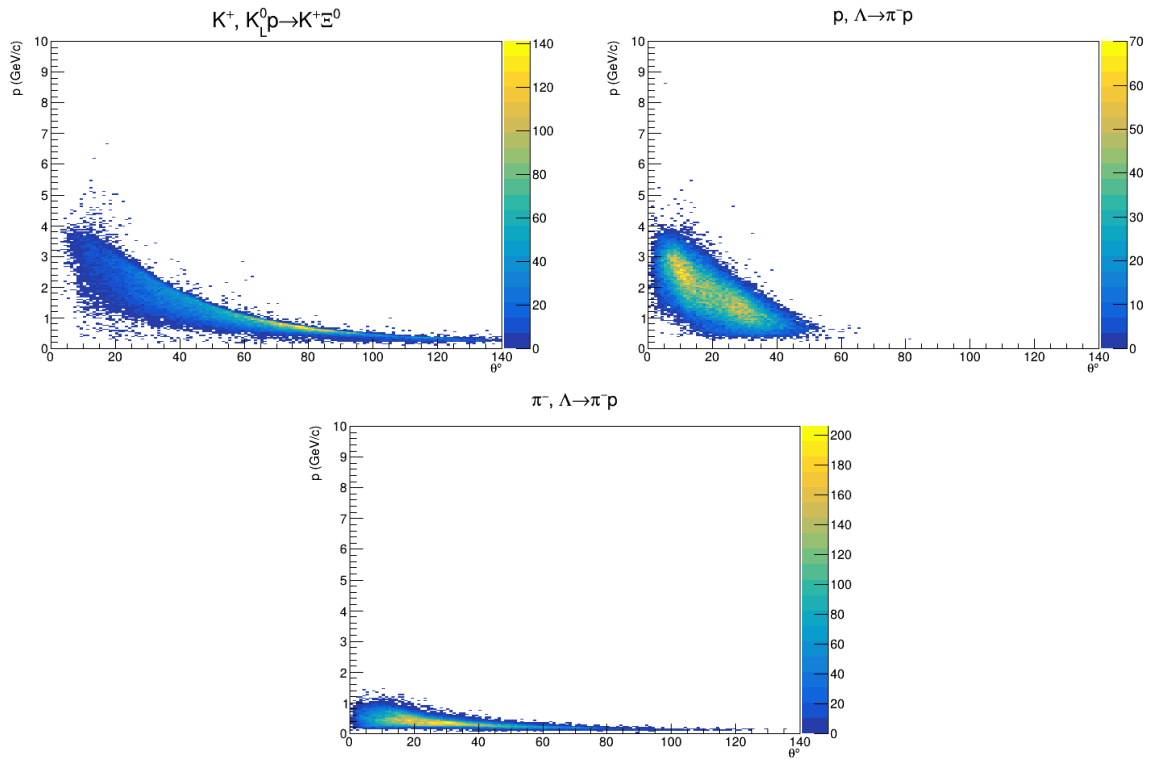As can be seen, we expect significant improvement over the existing data; see Figure 33.

Figure 30: Reconstructed θ vs momentum distributions for K (<u>top-left</u>), p (<u>top-right</u>), and π^- (<u>bottom</u>).
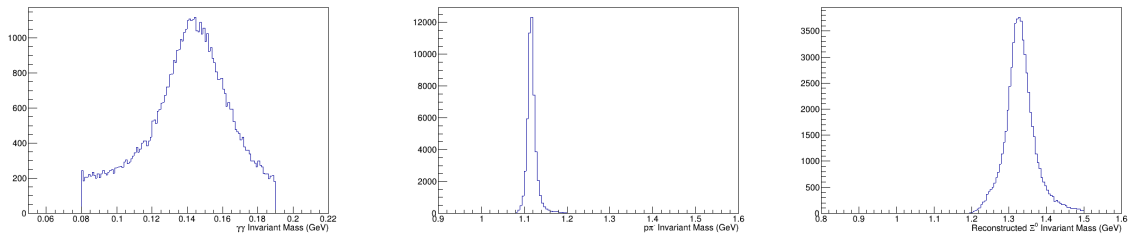

Figure 31: Reconstructed invariant masses of the π^0 (<u>left</u>), Λ (<u>middle</u>), and Ξ^0 (<u>right</u>).
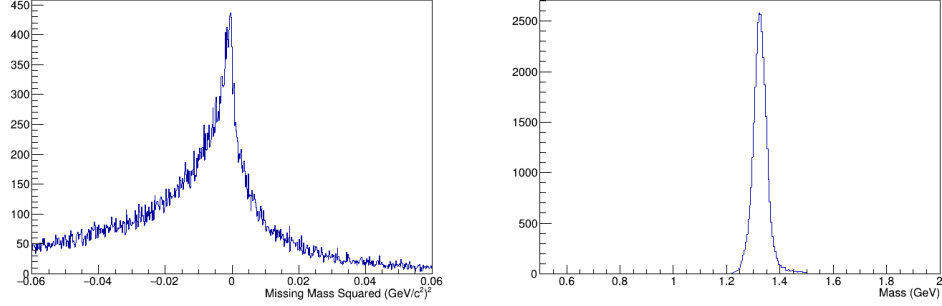
Figure 32: Missing mass squared of all final state particles. A cut is applied from $-0.3 < M_X < 0.2$ GeV^2(<u>left</u>) and Reconstructed invariant mass of the Ξ^0 after missing mass cut and invariant mass cuts on the π^0 and Λ (<u>right</u>).
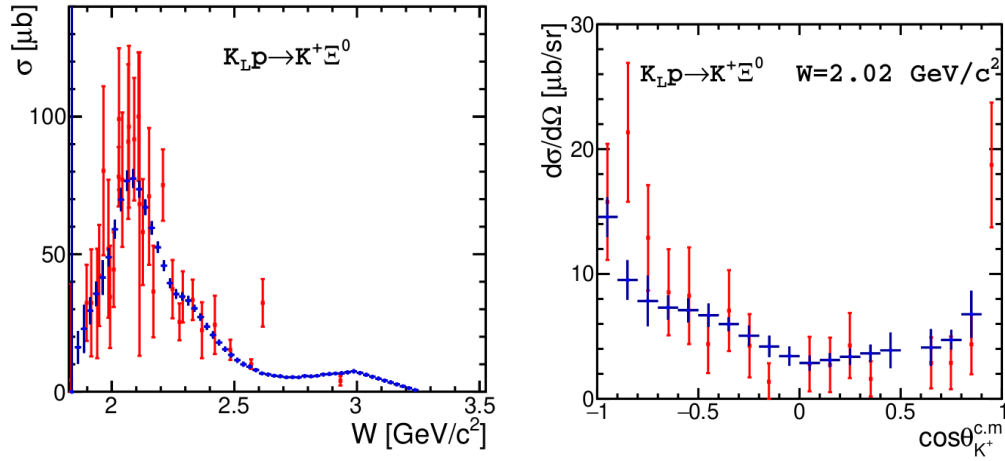

Figure 33: Total (<u>left</u>) and differential (<u>right</u>) cross section statistical uncertainty estimates (blue symbols) for fully reconstructed $K_L p \to K^+ \Xi^0$ events in comparison with existing data from Ref. [D. A. Sharov, V. L. Korotkikh and D. E. Lanskoy, Eur. Phys. J. A **47**, 109 (2011)].

4.3 $K_L p \to K_S p$ $(K_S \to \pi^+ \pi^-)$ and $K_L p \to K^+ n$

We plan to use these reactions to study their yield as a function of the beam momentum and/or W. The advantage of reaction $K_L p \to K_S p$ is that, due to the short lifetime of K_S ($c\tau = 2.9$ cm), it mostly results in three charged tracks that allow its vertex reconstruction inside a large volume of the LH2 target, as well as the total energy of the final particles. The total energy of three final particles may also be a powerful selection criterion.

The second reaction, $K_L p \to K^+ n$, has only one charged track in the final state, thus the actual vertex and the total energy cannot be reconstructed. However, the pseudo-vertex, defined as a DOCA between charged particle track and the beam axis, may be effective in event selection.

Various technical plots, such as momentum reconstruction and particle identification in CDC, common for both reaction $K_L p \to K_S p (K_S \to \pi^+ \pi^-)$ and $K_L p \to K^+ p$ are shown in Figs. 34 and 35. Reasonable sizes of the LH2 target are well reproduced by the $\pi^+ \pi^-$ vertex coordinate with a spatial resolution of 0.25 cm. A very strong correlation of the reconstructed momenta with the generated ones is clearly seen, while the pion-proton separation in CDC is reliable up to 1.2 GeV/c and the pion-kaon separation up to 0.8 GeV/c.

4.3.1 Reaction $K_L p \to K_S p$ $(K_S \to \pi^+ \pi^-)$

In Fig. 36, the reaction $K_L p \to K_S p$ $(K_S \to \pi^+ \pi^-)$ at beam momentum (0.3, 0.6) GeV/c is illustrated via Missing Mass (MM) and Effective Mass (EM) spectra of $\pi^+ \pi^-$ pairs. The effect of vertex cuts on the reconstruction of the recoil proton and K_S, respectively, is also demonstrated.

The MM spectrum, without vertex cuts, exhibits a distinct peak in proton mass with a resolution of 20 MeV, while the reconstruction efficiency, defined as the ratio of the number of events in the peak to the number of beam particles (K_L) followed by at least one track in the CDC, is 44%. The MM spectrum with vertex cuts shows about twice the proton peak resolution of 10 MeV. However, the reconstruction efficiency of the proton mass is about twice that of 22%.

The EM spectrum of pairs of $\pi^+ \pi^-$ with vertex cuts shows a sharp peak at the mass of K_S. The reconstruction efficiency is 25% (= 2500 / 1000), while the sensitivity (=peak/pedestal) is of 100. Without cuts K_S's are reconstructed with twice better efficiency of 50% (=6000/11000), while the sensitivity is unfortunately 10 times lower.

From these graphs, we conclude that reaction $K_L p \to K_S p$ $(K_S \to \pi^+ \pi^-)$ can be effectively used to scan its yield as a function of the K_L beam momentum within the (0.3, 0.6) GeV/c interval.
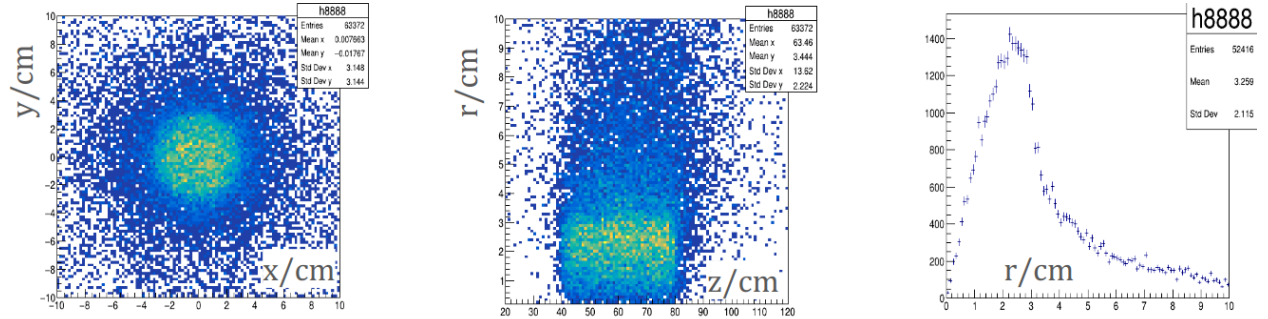

Figure 34: Reaction $K_L p \to K_S p$ $(K_S \to \pi^+ \pi^-)$. From left to right, K_s vertex X.vs.Y target profile, R.vs.Z profile, and R profile. The dimensions of the target are well reproduced. The radial resolution of vertex location is of 0.3 cm.

Reaction of $K_L p \to K_S p$ $(K_S \to \pi^+ \pi^-)$ at high beam momentum within (0.55, 4.55) GeV/c interval is less productive. The corresponding effective mass spectra and missing mass spectra of the $\pi^+ \pi^-$ pairs are
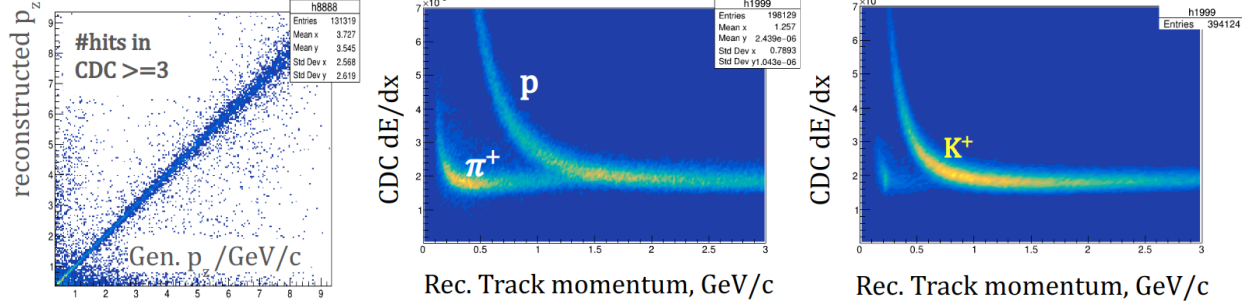
Figure 35: Reaction $K_L p \rightarrow K_S p$ $(K_S \rightarrow \pi^+\pi^-)$ and $K_L p \rightarrow K^+ n$. From left to right, momentum reconstruction in CDC, particle identification in CDC. A very strong correlation of reconstructed momenta with generated ones is clearly seen. The pion - proton separation in CDC is reliable up to ≈ 1.2 GeV/c, while pion-kaon separation - up to approximately 0.8 GeV/c.

shown in Fig. 37. The effect of vertex cuts on the reconstruction of the K_S and recoil proton are also shown in this figure.

With vertex cuts, the EM (K_S) resolution is of 10 MeV, while for a MM (proton) it is 25 MeV. In such a wide domain of beam momentum, the K_S reconstruction efficiency with vertex cuts is 14% while that for a proton in the final stat is 2% only.

The lower-left plot of this figure shows the scatter plot of EM ($\pi^+\pi^-$) vs. beam momentum. A good K_S signal is seen up to high beam momentum, while the proton signal is hardly seen after 2 GeV/c on the lower-right plot of Fig. 37.

4.3.2 Neutron Reconstruction in Reaction $K_L p \rightarrow K^+ n$

The reaction of $K_L p \rightarrow K^+ n$ is another remedy for studying the yield of the reaction as a function of the momentum of the beam in the domain (0.35, 0.55) GeV/c. The reconstructed missing-mass spectrum of K^+ with vertex cuts is shown in Fig. 38. The clean peak on the top-left plot points to recoil neutrons. With vertex cuts, the MM resolution is $15 - 20$ MeV. The efficiency of neutron reconstruction with vertex cuts is of 50%. However, in a high-momentum domain, the neutron peak is significantly wider and much less pronounced.

The plot top-right is for the energy loss in the CDC vs. beam momentum. Good K^+ separation from the pions is guaranteed up to high track momenta.

The two bottom plots show the x.vs.y and r.vs.z profiles of the LH2 target reconstructed from the pseudovertex coordinates determined as a DOCA between the track K^+ and the beam axis.

4.3.3 Backgrounds to $K_L p \rightarrow K^+ n$ Reaction.

There are many reactions that may contribute as background to the MM and EM mass spectra of the main reactions considered above. For example, the background may come from the main beam as a result of interactions such as $K_L p \rightarrow \pi^+ \Sigma^0(1192)$ or $K_L p \rightarrow \pi^+ \Lambda^0(1115)$. Both reactions have no threshold since the sum of the initial particles' masses is higher than that of the final particles. Therefore, both reactions may incorporate into MM(K^+) spectra of positive tracks at very low beam momenta, provided that the K^+'s are misidentified as π^+.

The MM spectra of the positive pions are shown in Fig. 39. for background reaction $K_L p \rightarrow \pi^+ \Sigma^0$ at two beam momentum intervals. In the momentum interval $0.25 < p_K < 0.55$ GeV/c the Missing Mass spectrum of π^+ with vertex cuts within the LH2 target (left plot) shows 64% of the reconstructed recoil Σ^0 with MM resolution of 6 MeV. With vertex cuts in the beam momentum interval $0.25 < p_K < 4.55$ GeV/c (right plot), the MM resolution is of 14 MeV, while the reconstruction efficiency is significantly lower - 18%. There
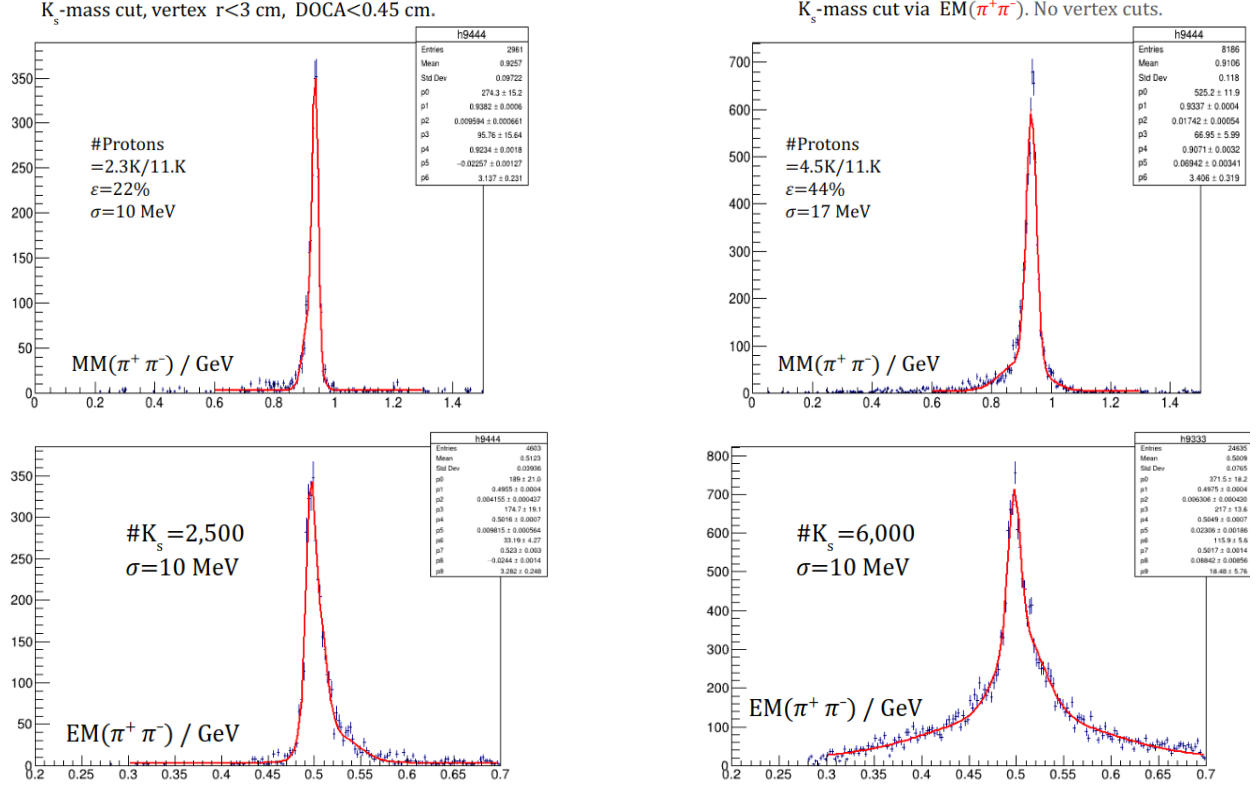
Figure 36: Reaction $K_L p \to K_S p$ $(K_S \to \pi^+\pi^-)$ at beam momentum (0.3, 0.6) GeV/c. Missing mass (top plots) and effective mass spectra (bottom plots) of $\pi^+\pi^-$ pairs and the effect of vertex cuts on the reconstruction of the recoil proton and K_S, respectively. Top-right: MM spectrum without vertex cuts; MM resolution is 17 MeV, while the reconstruction efficiency, defined as a ratio of the number of events in the peak to the number of beam particles (K_L), followed by at least one track in CDC, is 44%. Top-left: MM spectrum with vertex cuts; the MM resolution is about twice better – 10 MeV, while the reconstruction efficiency is about twice lower –22%. Bottom-left: Effective mass spectrum of $\pi^+\pi^-$ pairs with vertex cuts. The reconstruction efficacy K_S is 25% (= 2500/11000), while the sensitivity (=peak/pedestal) is of 100. Bottom-right: Without cuts K_S are reconstructed with the efficiency of 50% (=6000/11000) while the sensitivity is approximately 10 times lower.

is a very good separation between neutron and Σ^0, while the background level near the neutron mass is at the level of 0.001 of the total number of Σ^0.

A second source of background to $K_S(\pi^+\pi^-)$ in the final state may be a certain component of neutrons in the beam of K_L's by means of reactions $np \to K_S(\pi^+\pi^-)\Sigma^+ n$. The relevant neutron momentum interval $0.562 < p_n < 1.12$ GeV/c should have the same TOF values as the main K_L beam within (0.35, 0.55) GeV/c interval. However, the momentum of neutrons to make such reaction must be above 2.6 GeV/c, where the flux of the neutron component is approximately equal to or significantly lower than that of the main beam K_L. Moreover, the MM($\pi^+\pi^-$) should be above 2.13 GeV which is the sum of Σ^+ and neutron masses, that is, far away from the neutron mass. Therefore, we do not expect any problems with this channel, and this background will be analyzed in the future.
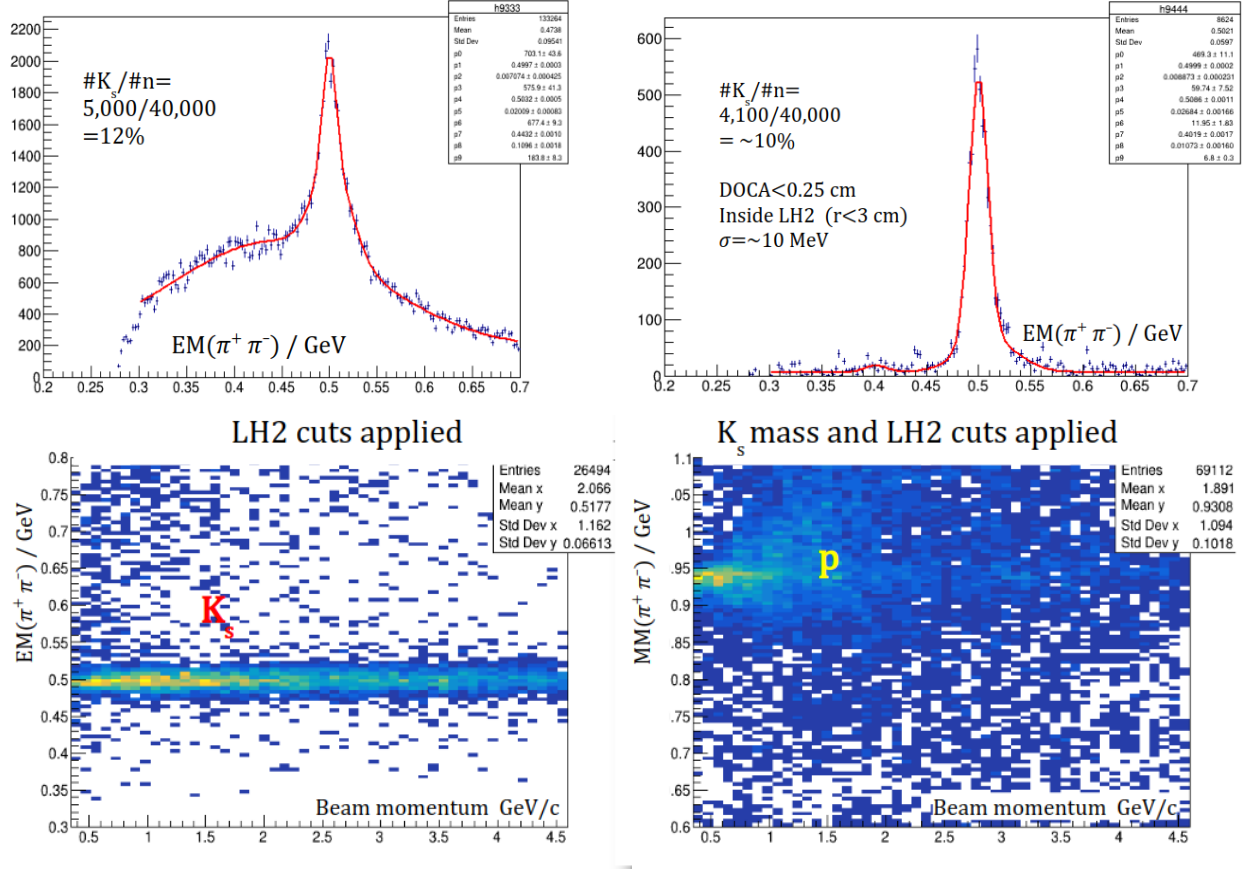
Figure 37: Reaction $K_L p \to K_S p$ $(K_S \to \pi^+\pi^-)$ at beam momentum (0.55, 4.55) GeV/c. Effective mass spectra (top-left) and missing mass spectra (top-right) of the pairs $\pi^+\pi^-$ and the effect of vertex cuts on reconstruction of the proton K_S and recoil, respectively. With vertex cuts, the EM resolution is 10 MeV, while for a final proton it is of 25 MeV. The reconstruction efficiency K_S with vertex cuts is of 14% while that for a proton in the final stat is of 2% only. The plot bottom-left is for EM $(\pi^+\pi^-)$ vs. beam momentum. A good K_S signal is seen up to high beam momentum, while the proton signal is hardly seen after 2 GeV/c $(MM(\pi^+\pi^-)$ vs. beam momentum).

4.3.4 Conclusive Remarks

All reactions considered may be reconstructed from events that have at least one charged track with an efficiency of 50%. Using the target cuts allows us to significantly reduce non-Gaussian tails of missing mass and effective mass distributions, which guarantees a good separation of these reactions. The main reconstruction parameters for several final states are listed in Table 4.

The area of low beam momenta is of special interest, and it looks like the GlueX detector is ideal for this beam momentum area, since the CDC allows enough good momentum resolution and acceptance for relatively slow particles, especially for reactions with 3 charged particles in the final state, when beam momentum is shared between several particles.
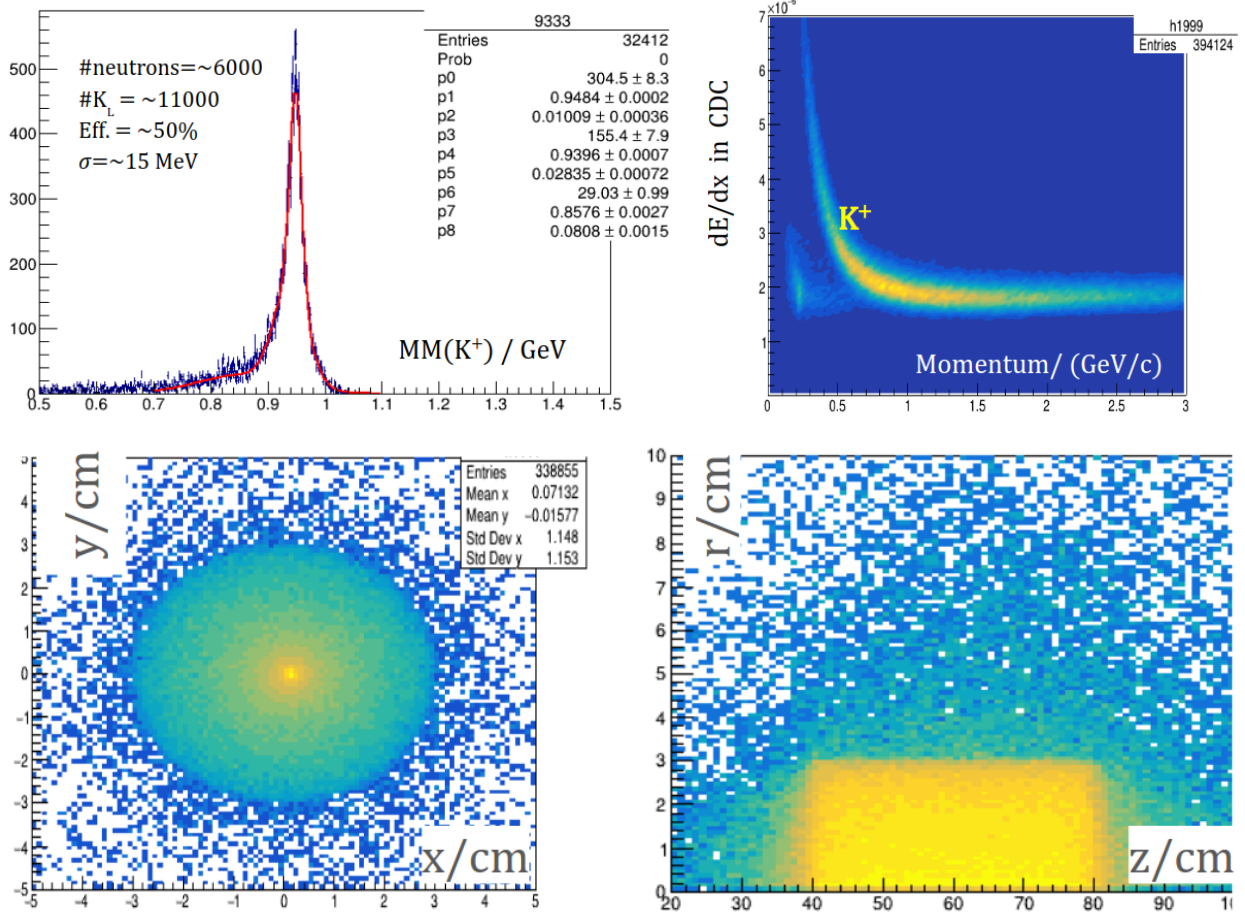
Figure 38: Reaction of $K_L p \to K^+ n$ at beam momentum (0.35, 0.55) GeV/c. The missing mass spectrum of K^+ (top-left) with vertex cuts points to recoil neutrons. With vertex cuts, the MM resolution is $15-20$ MeV. In such a narrow domain of beam momentum, the efficiency of neutron reconstruction, with vertex cuts, is of $\sim 50\%$. However, in a high-momentum domain, the neutron peak is significantly wider and much less pronounced. The plot top-right is for the energy loss in the CDC *vs.* beam momentum. Good K^+ separation from the pions is guaranteed up to high track momenta. The two bottom plots show the xvs.y and rvs.z profiles of the LH2 cryogenic target reconstructed from the vertex coordinate determined as a DOCA between the K^+ track and the beam axis.

Reaction	Efficiency/Resolution	Efficiency/Resolution
K_L momentum	(0.3, 0.6) GeV/c	(0.5, 5.0) GeV/c
$K_L p \to K_S...$	53 % / 10 MeV	14 % / 20 MeV
$K_L p \to K_S p$	44 % / 20 MeV	2 % / 25 MeV
$K_L p \to K^+ n$	50 % / 15 MeV	6 % / 50 MeV
$K_L p \to \pi^+ \Sigma$	64 % / 10 MeV	18 % / 15 MeV

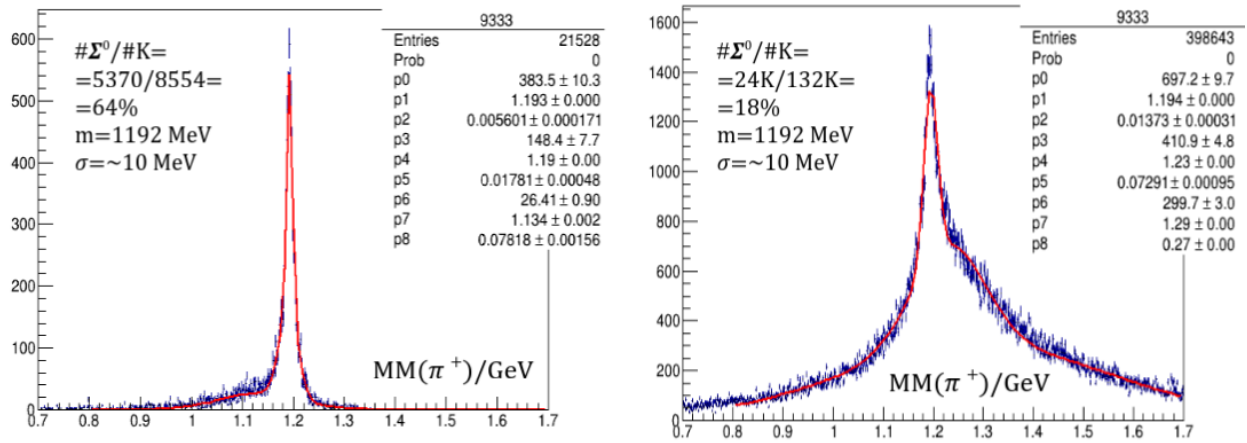Table 4:   Reconstruction efficiency and meson missing mass resolution.

35

Left plot labels:
- #Σ^0/#K= =5370/8554= =64% m=1192 MeV $\sigma=\sim$10 MeV
- MM(π^+)/GeV

Left stat box:
	9333
Entries	21528
Prob	0
p0	383.5 ± 10.3
p1	1.193 ± 0.000
p2	0.005601 ± 0.000171
p3	148.4 ± 7.7
p4	1.19 ± 0.00
p5	0.01781 ± 0.00048
p6	26.41 ± 0.90
p7	1.134 ± 0.002
p8	0.07818 ± 0.00156

Right plot labels:
- #Σ^0/#K= =24K/132K= =18% m=1192 MeV $\sigma=\sim$10 MeV
- MM(π^+)/GeV

Right stat box:
	9333
Entries	398643
Prob	0
p0	697.2 ± 9.7
p1	1.194 ± 0.000
p2	0.01373 ± 0.00031
p3	410.9 ± 4.8
p4	1.23 ± 0.00
p5	0.07291 ± 0.00095
p6	299.7 ± 3.0
p7	1.29 ± 0.00
p8	0.27 ± 0.00

Figure 39: Background reaction from kaon beam - $K_L p \to \pi^+ \Sigma^0$ - at two beam momentum intervals. In the momentum interval $0.25 < p_K < 0.55$ GeV/c the Missing Mass spectrum of π^+ with LH2 vertex cuts (left plot) shows 64% of reconstructed recoil Σ^0 with MM resolution of 6 MeV. With vertex cuts in the beam momentum interval $0.25 < p_K < 4.55$ GeV/c (right plot), the MM resolution is of 14 MeV, while the reconstruction efficiency is significantly lower - 18%.

4.4 $K_L p \to K^*(892)p \to K^+\pi^- p$

$K\pi$ scattering is the simplest hadronic reaction involving an s quark, and it plays a crucial role in understanding non-perturbative QCD. Despite its importance, even fundamental low-energy parameters, such as the scattering length in Chiral Perturbation Theory, are not yet satisfactorily determined. In the KLF experiment, by scattering a K_L beam of protons and analyzing the reaction where a pion is exchanged in the t channel, valuable information about $K\pi$ scattering can be obtained. This new data from the KLF experiment will be essential in addressing these unresolved issues.

Figure 40 shows the dominant leading-order diagram at low Mandelstam t. The $K\pi$ scattering information is encoded in the enclosed $K\pi K\pi$ vertex.
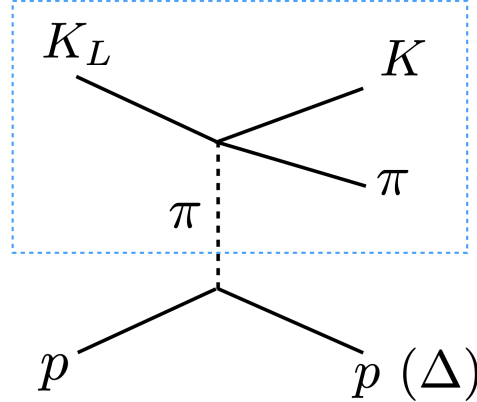
Figure 40: Dominant diagram at low Mandelstam t. The information on the $K\pi$ scattering (enclosed by the blue dotted line) can be accessed using this t-channel reaction.

4.4.1 Generator

The Regge-pole model [G. V. Dass and C. D. Froggatt, Nucl. Phys. B **10**, 151 (1969)] is used to generate events for the reaction $K_L p \to K^{*0}(892)p$, where the helicity amplitudes for the crossed t channel are written as follows:

$$f^t_{\lambda_2\lambda_4,\lambda_1\lambda_3} = \frac{1 + \tau \exp\left[-i\pi\alpha(t)\right]}{\sin\left[\pi\alpha(t)\right]} \exp\left[-\frac{1}{2}i\pi((\lambda_1 - \lambda_3) - (\lambda_2 - \lambda_4))\right] \gamma_{\lambda_3\lambda_1}(t)\gamma_{\lambda_4\lambda_2}(t) \left(\frac{s}{s_0}\right)^{\alpha(t)}.$$

Figure 41 shows the leading order Feynman diagram where the π and a_2 Regge pole trajectories are exchanged in the t-channel to generate a vector meson $K^{*0}(892)$. The $K^{*0}(892)$ resonance decays to the $K\pi$ system uniformly in the phase space.

In the original paper, the amplitudes for the reactions $K^\pm p \to K^{*\pm}p$ are calculated, and we assume this non-charge-exchange reactions have the same amplitudes as the reaction $K_L p \to K^{*0}p$. The π Regge-pole exchange amplitudes are dominant and a_2 trajectory is taken into account as well. Also, the even signature ($\tau = +1$) natural parity isoscalar trajectory (called P'' in the paper) plays an important role in the non-charge-exchange reactions. The parameters for the vertex functions $\gamma_{\lambda_3\lambda_1}(t)\gamma_{\lambda_4\lambda_2}(t)$ and the Regge trajectory of P'' ($\alpha_{P''}(t) = \alpha_0 + \alpha_1 t$) have been determined from the $K^\pm p \to K^{*\pm}p$ data.

The Mandelstam t and $M(K^+\pi^-)$ distributions generated are shown in Figure 42.

4.4.2 Event Reconstruction

The event reconstruction was performed using the standard analysis software of GlueX. The momentum-momentum distribution of the generated final-state particles and the momentum-angular distribution recon-
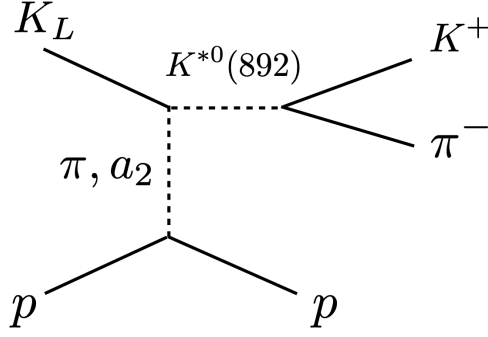
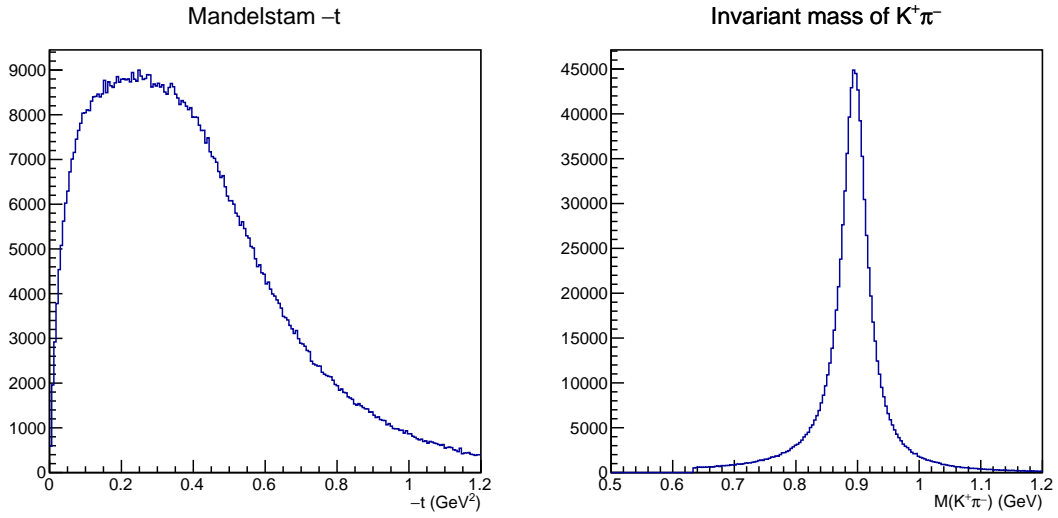Figure 41: The leading order diagram for the reaction $K_L p \rightarrow K^{*0}(892)p$.

Figure 42: Mandelstam t distribution and $M(K^+\pi^-)$ distribution.

structed by the GlueX detector are as shown in Figures 43 and 44, respectively. Here, all final-state particles are detected by the GlueX detector, and the $K^+\pi^- p$ event is exclusively reconstructed.
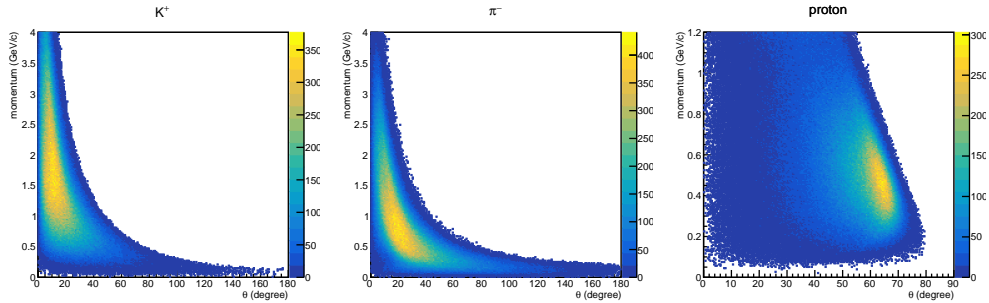

Figure 43: Generated momentum vs angle distribution of the final-state particles

The event reconstruction efficiencies as a function of Mandelstam t and the invariant mass of $K^+\pi^-$ are
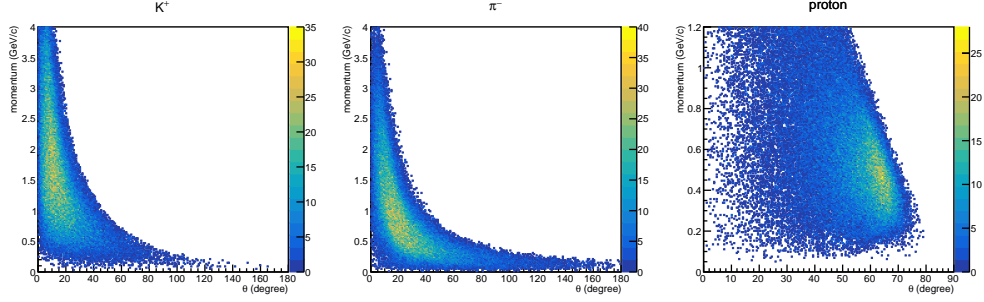
38

Figure 44: Reconstructed momentum vs angle distribution of the final-state particles
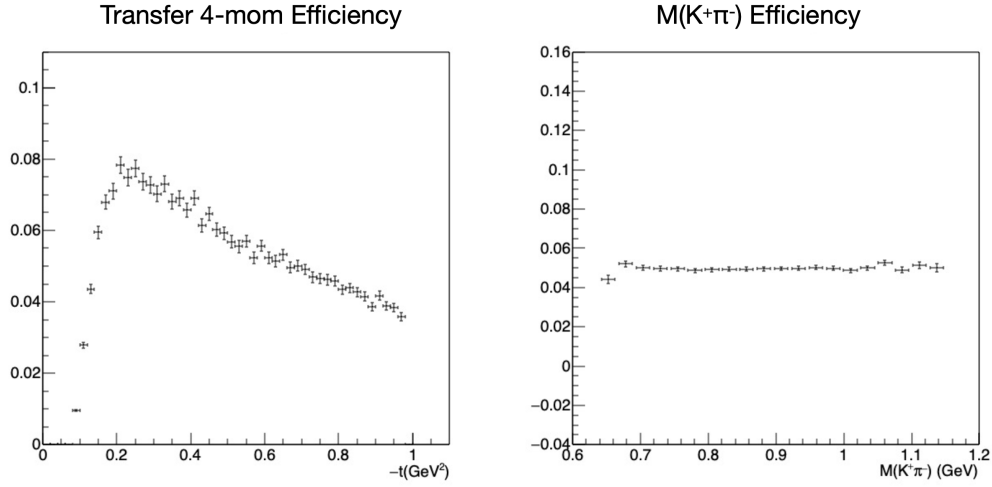
shown in Figure 45.

Figure 45: Efficiencies as a function of Mandelstam t (left) and invariant mass of $K^+\pi^-$ (right).

The expected number of events can be calculated as follows:

$$N(\vec{p}) = \sigma_{K^*}(\vec{p}) \times \text{BR}(K^* \to K^+\pi^-) \times \int \mathcal{L}\,dt \times \epsilon_{\text{tot}}(\vec{p}) \,,$$

where $\vec{p}$ represents the beam momentum, σ denotes the total cross section for K^* production, $\text{BR}(K^*(892) \to K^+\pi^-)$ is the branching ratio (approximately 100%), $\epsilon_{\text{tot}}(\vec{p})$ is the total efficiency function dependent on the beam momentum and $\int \mathcal{L}\,dt$ is the integrated luminosity over time, defined as:

$$\int \mathcal{L}\,dt = n_K \times n_t \times T \,.$$

Here, n_K is the rate of K_L incident on the target per second, n_t is the number of scattering centers per unit area, and T is the total live time of the detector.

Figure 46 shows the number of events exclusively reconstructed for 100 days of KLF running. The previous SLAC statistics are also shown for comparison.
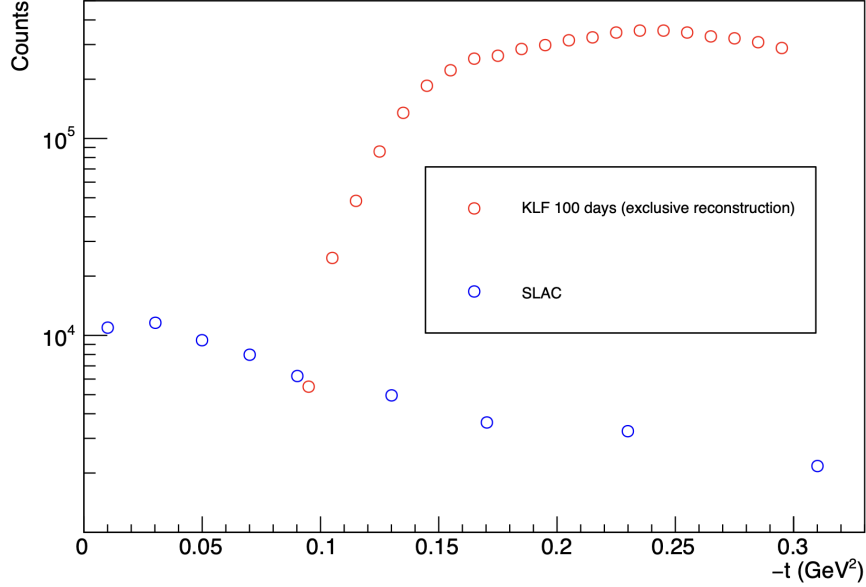
Figure 46: Expected yield as a function of Mandelstam t (<u>left</u>) and invariant mass of $K^+\pi^-$ (<u>right</u>).

4.4.3 Δ Recoil Reaction

The reaction $K_L p \to K^-\pi^0\Delta^{++}$ was simulated using the theoretical scattering amplitude and phase $K\pi$ provided by [J. R. Pelaez and A. Rodas, Phys. Rev. D **93**, 074025 (2016)]. Figure 47 shows the leading order diagram and the Mandelstam distribution generated t is shown to the left of Figure 48. The generated P wave was then weighted using the relativistic Breit-Wigner resonance $K^*(892)^-$, as shown in Figure 48. Figure 49 presents graphs of the momentum versus polar angle distributions for K^-, π^+, proton, and π^0 from both generated events (<u>top</u>) and reconstructed events (<u>bottom</u>). Here, all final-state particles are detected by the GlueX detector, and $K^-\pi^0 p\pi^+$ events are exclusively reconstructed.
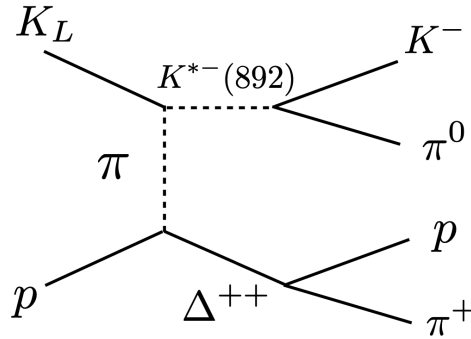

Figure 47: The leading order diagram for the reaction $K_L p \to K^{*-}(892)\Delta^{++}$.

Events were processed through standard Hall-D GEANT simulation, including the GlueX detector and momentum smearing, and particle reconstruction was performed using the JANA framework.

An efficiency study of the Mandelstam variables t and $M(K^-\pi^0)$ was conducted to assess the potential improvements in the study of the system $K\pi$ using KLF. The simulation results indicate that the total
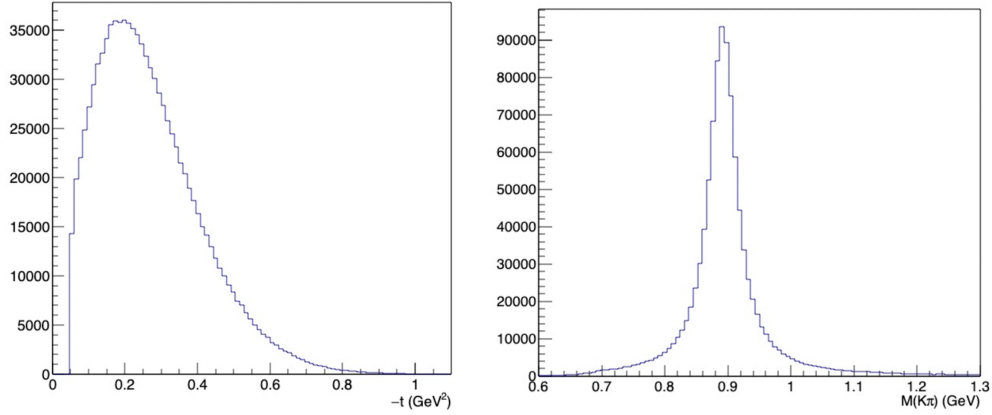
Figure 48: Mandelstam t (<u>left</u>) and $M(K^-\pi^0)$ (<u>right</u>) distributions.

Generated distributions
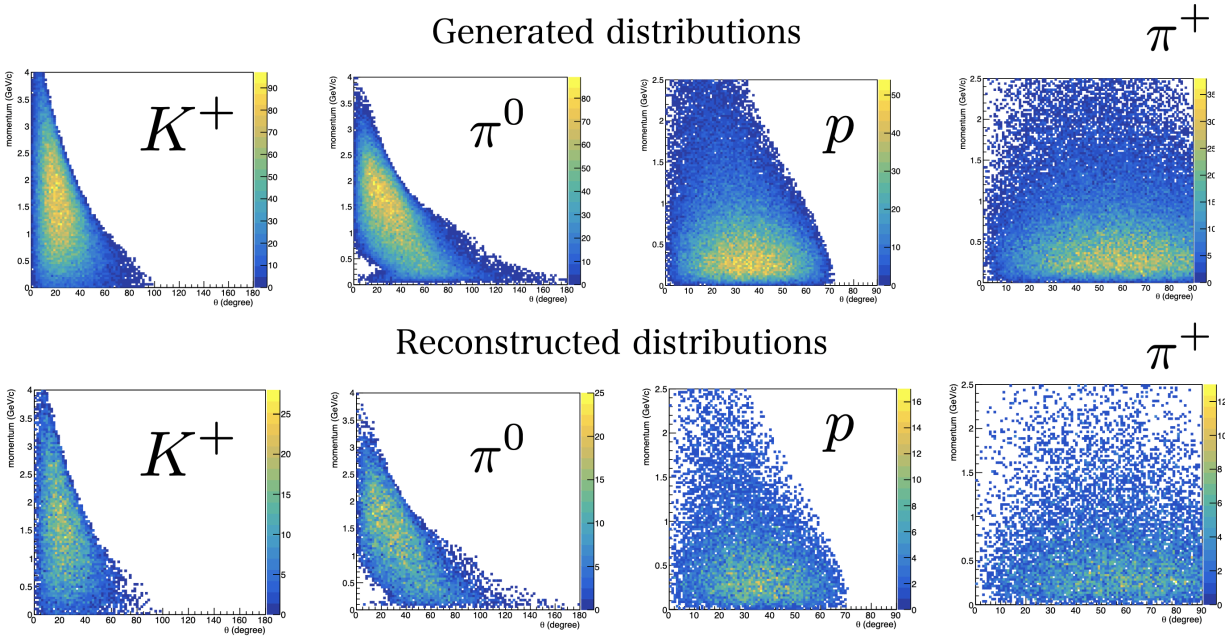

Reconstructed distributions

Figure 49: Generated momentum vs angle distribution of the final-state particles (<u>top</u>) and reconstructed momentum vs angle distribution of the final-state particles (<u>bottom</u>).

integrated efficiency for the reaction $K_L p \to K^- \pi^0 \Delta^{++}$ is approximately 8%, with this value remaining consistent in nearly all bins of t. Furthermore, the efficiency of the invariant mass $K^- \pi^0$ is uniform throughout the entire mass range, as shown in Figure 50.

With the efficiency shown in Figure 50 and the beam flux, we estimate the expected number of Δ recoil events for 100 days of KLF operation, as shown in Figure 51. We expect roughly 0.9 M events, and this statistic is enough to perform a partial-wave analysis.
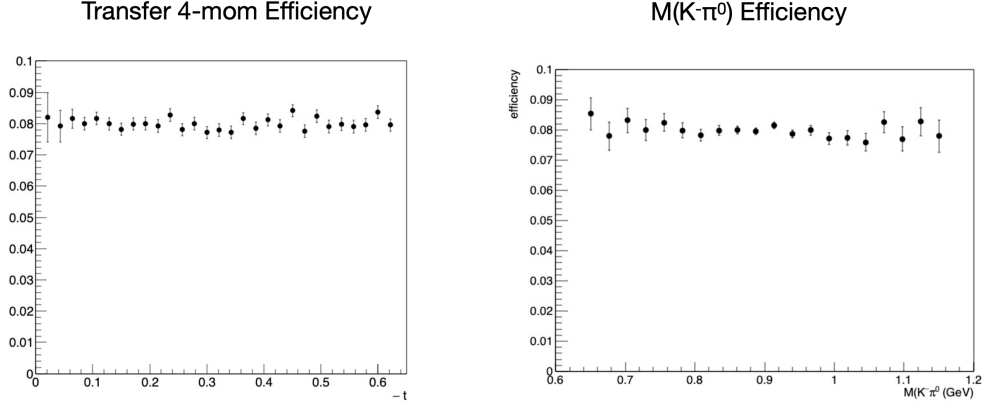
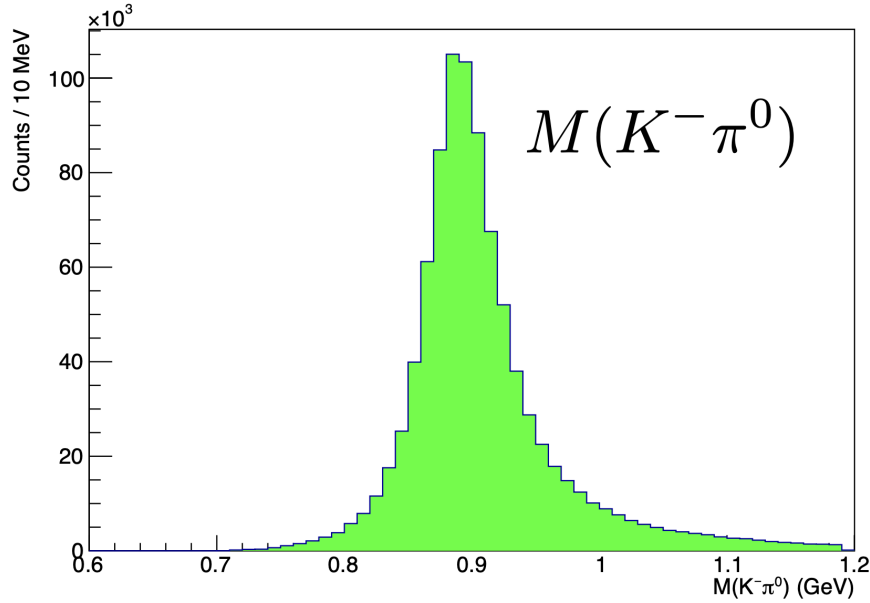Figure 50: Efficiencies as a function of Mandelstam t (left) and invariant mass of $K^-\pi^0$ (right).

Figure 51: Expected distribution of the $K^-\pi^0$ invariant mass after 100 days of run.

4.4.4 Conclusive Remarks

Several critical aspects of $K\pi$ scattering remain unresolved, particularly the existence of the scalar κ meson and the discrepancies between experimental data and theoretical predictions. Addressing these issues is essential not only to complete the scalar meson but also to improve our understanding of the SU(3) chiral perturbation theory and the underlying mechanisms of QCD's spontaneous chiral symmetry breaking. The current limitations of existing data, which start at 750 MeV, underscore the need for new low-energy measurements near the 635 MeV threshold. The upcoming KLF data, with its anticipated improvements in both energy range and statistical accuracy, will be pivotal in resolving these long-standing questions and advancing our understanding of meson dynamics.

5   KLF Technical Coordinators

Coordinators [https://wiki.jlab.org/klproject/index.php/Technical_Coordinators] have the appropriate skills for:

- Turning the equipment on and setting it up for the run.

- Performing operations during the run.

- Data monitoring.

- Performing and/or consulting on the calibration of the detector during and after the run.

1. **Tech Coordinator from Hall D**: Hovanes Egiyan (JLab).

2. **Calorimetry**: Sasha Somov (JLab) and Igal Jaegle (JLab).

3. **CDC**: Simon Taylor (JLab), Beni Zihlmann (JLab), and Axel Schmidt (GWU).

4. **FDC**: Lubomir Pentchev (JLab) and Simon Taylor (JLab).

5. **Tracking**: Simon Taylor (JLab) and Keigo Mizutani (RCNP, Osaka U.).

6. **PID**: Simon Taylor (JLab).

7. **Time-of-Flight**: Beni Zihlmann (JLab).

8. **Start Counter**: Joerg Reinhold (FIU).

9. **CPS**: Hovanes Egiyan (JLab).

10. **Flux Monitor**: Michail Bashkanov (UoY) and Stuart Fegan (UoY).

11. **Cryo Target**: Chris Keith (JLab).

12. **Trigger**: Sasha Somov (JLab).

13. **DIRC**: Justin Stevens (W&M).

14. **Beamline**: Edy Nissan (JLab), Richard Jones (UConn), Hovanes Egiyan (JLab), Bill Briscoe (GWU), Gabriel Niculescu (JMU), and Axel Schmidt (GWU).

15. **FSD Detectors and "Active Collimator"**: Richard Jones (UConn) and Hovanes Egiyan (JLab).

16. **Online Software and DAQ**: Sergey Furletov (JLab).

17. **Offline Software**: Alexander Austregesilo (JLab).

18. **Data Production and Monitoring**: Alexander Austregesilo (JLab), Igal Jaegle (JLab), and Olga Cortes (GWU).

19. **Detector Calibration**: Sean Dobbs (FSU).

20. **Engineering/Integration**: Tim Whitlath (JLab).

21. **Electronics**: Fernando Barbosa (JLab).

22. **Monitoring of the Radiation Environment**: Hovanes Egiyan (JLab), Alexander Deur (JLab), and Vitaly Baturin (ODU).

6 KLF Personnel

KLF Planning Committee has **39** members (experimental group representatives). JLab PAC48 (2020) approved the KLF experiment for **200** days of running time. It means that we will run **400** calendar days. So, we must cover **2400** shifts. The KLF personnel is enough to cover **5** blocks of shifts per KLF Collaboration member for this running time.

For calibration of the proton target data, it is expected to require **7** FTE of effort from the Collaboration, in consultation with the technical coordinators. Specific personnel for these tasks will be identified closer to the start of K_L beam operations, since it is expected to be more than **2** years until they begin.

For the physics topics discussed in the KLF proposal, **14** institutions have expressed an intention to contribute to the Hyperon Spectroscopy part and **7** institutions have expressed an intention to contribute to the Kaon Spectroscopy part, with **6** institutions intending to contribute to both physics topics. A detailed distribution of reaction channels to analyzers will be done closer to when data collection begins.